

Euler inversion: Locating sources of potential-field data through inversion of Euler's homogeneity equation

Leonardo Uieda¹, Gelson Ferreira Souza-Junior¹, India Uppal², Vanderlei Coelho Oliveira Jr.³

¹ Universidade de São Paulo, Brazil; ² University of Liverpool, UK; ³ Observatório Nacional, Brazil;

Submitted for publication to *Geophysical Journal International* on 2024/12/20.

Keywords: Gravity anomalies and Earth structure; Magnetic anomalies: modelling and interpretation; Inverse theory;

¹ Abstract

² Locating the sources of observed disturbances in potential-field data is a challenging problem due
³ to the non-unique nature of the inverse problem. The Euler deconvolution method was created
⁴ to solve this issue, particularly for idealized sources (such as spheres, planar vertical dykes).
⁵ Euler deconvolution has become widely used in potential-field methods due, in large part, to its
⁶ low computational cost and ease of implementation into software. However, it is widely known
⁷ that Euler deconvolution suffers from some shortcomings: 1) non-uniqueness of the solution with
⁸ respect to the depth of the source and the structural index (a parameter that represents the
⁹ idealised shape of the source); 2) sensitivity to short-wavelength noise in the data derivatives
¹⁰ which are used as inputs for the method. Here, we present a new method called *Euler inversion*
¹¹ which is a reformulation of the inverse problem of Euler's homogeneity equation as an implicit
¹² mathematical model rather than a parametric one. Euler inversion is a constrained, non-linear
¹³ inverse problem capable of estimating both the model parameters (location of the source and
¹⁴ constant base level) and the predicted data (potential field and its derivatives). We show that
¹⁵ Euler inversion is less sensitive than Euler deconvolution to short-wavelength noise and to the
¹⁶ presence of interfering sources in the data window. By also estimating the predicted data, Euler
¹⁷ inversion is also able to estimate the best integer structural index to be used for inversion. Our

¹⁸ results show that the estimated structural index minimizes the data misfit and coincides with
¹⁹ those of the simulated sources. Furthermore, most matrices involved in the method are either
²⁰ sparse or diagonal, making Euler inversion computationally efficient. Tests on synthetic data and
²¹ a real aeromagnetic dataset from Rio de Janeiro, Brazil, demonstrate the effectiveness of Euler
²² inversion to delineate sources with variable geometries and correctly estimate their depths.

²³ 1 Introduction

²⁴ Estimating the depths of the sources of measured anomalies is a common challenge in potential-
²⁵ field geophysics. One of the most widely used techniques for providing depth estimates is Euler
²⁶ deconvolution ([Reid et al., 1990](#); [Thompson, 1982](#)). Its widespread adoption is due, in large
²⁷ part, to its low algorithmic complexity and fast computation times, both of which are orders of
²⁸ magnitude smaller than solutions from 3D inverse problems. As a result, Euler deconvolution
²⁹ is widely available in both commercial and open-source software ([Uieda et al., 2013, 2014](#)).
³⁰ Unfortunately, this popularity has also led to abuses of the method, as reported in [Reid and](#)
³¹ [Thurston \(2014\)](#) and [Reid et al. \(2014\)](#).

³² Euler deconvolution is a method that assumes potential-field data are generated by idealized
³³ sources, such as dikes, dipoles, or pipes. The geometry of these sources is characterized by the
³⁴ structural index, a parameter that must be an integer to retain physical significance ([Reid and](#)
³⁵ [Thurston, 2014](#); [Stavrev and Reid, 2007](#)). The technique involves performing a least-squares
³⁶ inversion of Euler's homogeneity equation multiple times, in a moving window scheme. Each
³⁷ inversion estimates the base level, a constant shift in the data, and also the coordinates of a
³⁸ single idealized source potentially present within the study area.

³⁹ It is well known that Euler deconvolution suffers from some limitations, of which we highlight:

- ⁴⁰ **1. Separation of reliable and spurious solutions:** The moving window scheme adopted
⁴¹ in Euler deconvolution generates many estimated positions which are considered spurious
⁴² and must be removed. Most of the spurious solutions happen when the moving window
⁴³ either lacks significant potential-field anomalies or only contains a truncated anomaly.

44 FitzGerald et al. (2004) and Melo and Barbosa (2020) provide overviews of the many
45 existing methods that have been developed to remove spurious solutions.

46 **2. Sensitivity to high-frequency noise:** Random noise in the data is usually of high-
47 frequency, which gets amplified in the derivative calculations. Since the field derivatives
48 are used in the Jacobian matrix of the least-squares inversions, errors in the derivatives
49 will have a large impact on the solution. Paštěka et al. (2009), Saleh and Paštěka (2012),
50 and Florio et al. (2014) recommend using regularised derivatives or other smoothing
51 techniques to reduce the noise amplification and obtain more reliable solutions. This is
52 also why Euler deconvolution variants that rely on higher-order derivatives, like tilt-Euler
53 deconvolution (Huang et al., 2019; Salem et al., 2007) and AN-EUL (Salem and Ravat,
54 2003), present a larger dispersion of estimated positions and are more sensitive to noise
55 in general. Methods like finite-difference Euler deconvolution (Gerovska et al., 2005) and
56 ratio-Euler deconvolution (Huang et al., 2022) were specifically developed to avoid the use
57 of higher-order derivatives because of this noise-sensitivity issue.

58 **3. Correlation of the estimated depth and the structural index:** Silva et al. (2001)
59 demonstrated that the estimated depth from Euler deconvolution is directly correlated
60 with the structural index used. The higher the structural index, the larger the estimated
61 depth. This makes it very important to know the best integer structural index for the type
62 of source being interpreted. Some Euler deconvolution variants have been developed that
63 are able to estimate the structural index (e.g., Florio and Fedi, 2013; Florio et al., 2014;
64 Gerovska et al., 2005; Melo and Barbosa, 2018; Melo et al., 2013; Salem and Ravat, 2003;
65 Salem et al., 2007; Silva and Barbosa, 2003). However, most of them estimate real-valued
66 structural indices instead of integers, are sensitive to noise, and tend to underestimate the
67 structural index under realistic noise and signal overlap scenarios.

68 We aim to tackle the issues of sensitivity to noise and structural index estimation by
69 reformulating the inverse problem of solving Euler's homogeneity equation. The issue of noise
70 sensitivity can be traced back to the presence of data derivatives in the Jacobian matrix,

71 which generally contain larger amounts of noise than the original potential field. We propose
72 formulating the inverse problem as a non-linear optimisation with Euler's equation as a constraint.
73 This is similar to "total least-squares" in statistics (Van Huffel and Vandewalle, 1991) and
74 "combined adjustment" in geodesy (Vanícek and Krakiwsky, 1986). Another advantage of this
75 new formulation is the ability to calculate predicted data for the potential-field and its three
76 derivatives, which is impossible in Euler deconvolution and all of its variants. We call our new
77 method "Euler inversion".

78 2 Methodology

79 Starting with Thompson (1982) and Reid et al. (1990), Euler's equation has been used to
80 estimate the source positions of gravity and magnetic data. In this section, we will review the
81 solution of Euler's equation for the source location (x_o, y_o, z_o) by Euler deconvolution (Reid
82 et al., 1990) and then present a new method, called *Euler inversion*, for solving Euler's equation
83 using total least-squares.

84 We start with Euler's homogeneity equation

$$(x - x_o)\partial_x f + (y - y_o)\partial_y f + (z - z_o)\partial_z f + \eta(f - b) = 0 , \quad (1)$$

85 in which f is a homogeneous function (in this case, a potential-field), ∂_α is the derivative operator
86 in the α dimension, (x, y, z) are the coordinates of the observation point, (x_o, y_o, z_o) are the
87 coordinates of the field source, b is the base level representing a constant shift in the field, and η is
88 the structural index, which is related to the nature of the source and how its potential-field values
89 decay with distance (Reid and Thurston, 2014; Ruddock et al., 1966). The coordinate system is
90 defined with x pointing eastward, y pointing northward, and z pointing upward. Equation 1
91 relates the coordinates of the source with the potential field and its gradient observed at the
92 point (x, y, z) .

93 Given N observations points in which we have measured f and its gradient (for a total $4N$
94 data), we can define the system of N equations and 4 unknowns

$$\begin{aligned}
(x_1 - x_o) \partial_x f_1 + (y_1 - y_o) \partial_y f_1 + (z_1 - z_o) \partial_z f_1 + \eta(f_1 - b) &= 0 \\
(x_2 - x_o) \partial_x f_2 + (y_2 - y_o) \partial_y f_2 + (z_2 - z_o) \partial_z f_2 + \eta(f_2 - b) &= 0 \\
&\vdots
\end{aligned} \tag{2}$$

$$(x_N - x_o) \partial_x f_N + (y_N - y_o) \partial_y f_N + (z_N - z_o) \partial_z f_N + \eta(f_N - b) = 0$$

95 Both Euler deconvolution and Euler inversion aim to solve the equation system above to estimate
96 the parameter vector

$$\mathbf{p} = \begin{bmatrix} x_o & y_o & z_o & b \end{bmatrix}^T. \tag{3}$$

97 2.1 Euler deconvolution

98 Euler deconvolution starts by rearranging Equation 2 to place the parameters on the left-hand
99 side and all other terms on the right-hand side. This is an attempt to form a *parametric model*
100 which results in the equation system

$$\begin{aligned}
-x_o \partial_x f_1 - y_o \partial_y f_1 - z_o \partial_z f_1 - \eta b &= -x_1 \partial_x f_1 - y_1 \partial_y f_1 - z_1 \partial_z f_1 - \eta f_1 \\
-x_o \partial_x f_2 - y_o \partial_y f_2 - z_o \partial_z f_2 - \eta b &= -x_2 \partial_x f_2 - y_2 \partial_y f_2 - z_2 \partial_z f_2 - \eta f_2 \\
&\vdots \\
-x_o \partial_x f_N - y_o \partial_y f_N - z_o \partial_z f_N - \eta b &= -x_N \partial_x f_N - y_N \partial_y f_N - z_N \partial_z f_N - \eta f_N
\end{aligned}, \tag{4}$$

101 which can be written in matrix form as

$$\underbrace{\begin{bmatrix} -\partial_x f_1 & -\partial_y f_1 & -\partial_z f_1 & -\eta \\ -\partial_x f_2 & -\partial_y f_2 & -\partial_z f_2 & -\eta \\ \vdots & \vdots & \vdots & \vdots \\ -\partial_x f_N & -\partial_y f_N & -\partial_z f_N & -\eta \end{bmatrix}}_{\mathbf{A}} \underbrace{\begin{bmatrix} x_o \\ y_o \\ z_o \\ b \end{bmatrix}}_{\mathbf{p}} = \underbrace{\begin{bmatrix} -x_1 \partial_x f_1 - y_1 \partial_y f_1 - z_1 \partial_z f_1 - \eta f_1 \\ -x_2 \partial_x f_2 - y_2 \partial_y f_2 - z_2 \partial_z f_2 - \eta f_2 \\ \vdots \\ -x_N \partial_x f_N - y_N \partial_y f_N - z_N \partial_z f_N - \eta f_N \end{bmatrix}}_{\mathbf{c}}, \tag{5}$$

102 in which \mathbf{A} is the Jacobian matrix of Euler's equation (Equation 1) concerning the parameters

¹⁰³ (Equations 3) and \mathbf{c} is a *pseudo-data vector*.

¹⁰⁴ The solution proposed by Thompson (1982) and Reid et al. (1990) is a least-squares estimate
¹⁰⁵ of \mathbf{p}

$$\hat{\mathbf{p}} = (\mathbf{A}^T \mathbf{A})^{-1} \mathbf{A}^T \mathbf{c} . \quad (6)$$

¹⁰⁶ The covariance matrix of the solution \mathbf{C}_p is obtained through standard error propagation
¹⁰⁷ assuming that the only variable with uncertainty is the pseudo-data vector \mathbf{c}

$$\mathbf{C}_p = \hat{\sigma}_0^2 (\mathbf{A}^T \mathbf{A})^{-1} , \quad (7)$$

¹⁰⁸ in which $\hat{\sigma}_0^2 = \|\mathbf{c} - \mathbf{Ap}\|^2 / (N - 4)$ is the reduced chi-squared statistic and an estimate of the
¹⁰⁹ variance factor of \mathbf{c} .

¹¹⁰ The solution in Equation 6 above is valid only if the contents of the Jacobian matrix \mathbf{A} are
¹¹¹ assumed to be error-free. As can be seen from Equation 5, the Jacobian contains the derivatives
¹¹² of f , which are often computed numerically by finite-differences or Fourier transforms and
¹¹³ are known to amplify the high-frequency random noise in the data. This presents a problem,
¹¹⁴ particularly for the estimation of z_o , which has been widely explored in the literature (Florio
¹¹⁵ et al., 2014; Melo and Barbosa, 2020; Paštka et al., 2009; Silva et al., 2001).

¹¹⁶ 2.2 Euler inversion: Formulation

¹¹⁷ Euler inversion starts by assigning the potential-field f to a $N \times 1$ vector

$$\mathbf{f} = \begin{bmatrix} f_1 & f_2 & \cdots & f_N \end{bmatrix}^T . \quad (8)$$

¹¹⁸ We can then define a $4N \times 1$ *data vector* which contains all of the values of f and its gradient

$$\mathbf{d} = \begin{bmatrix} \mathbf{f}^T & \nabla_x \mathbf{f}^T & \nabla_y \mathbf{f}^T & \nabla_z \mathbf{f}^T \end{bmatrix}^T . \quad (9)$$

¹¹⁹ in which ∇_α is the gradient operator in the α dimension.

120 Next, we formulate the $N \times 4$ equation system from Euler's equation (Equation 2) as a
 121 non-linear function of both parameters and data

$$\mathbf{e}(\mathbf{p}, \mathbf{d}) = \mathbf{0} , \quad (10)$$

122 which is known in geodesy as an *implicit mathematical model* (Vanícek and Krakiwsky, 1986).

123 We then wish to solve the following constrained optimisation problem with non-linear equality
 124 constraints to estimate both the parameters and the predicted data simultaneously

$$\begin{aligned} \min_{\mathbf{p}, \mathbf{d}} \quad & \phi(\mathbf{d}) = [\mathbf{d}^o - \mathbf{d}]^T \mathbf{W} [\mathbf{d}^o - \mathbf{d}] \\ \text{subject to} \quad & \mathbf{e}(\mathbf{p}, \mathbf{d}) = \mathbf{0} , \end{aligned} \quad (11)$$

125 in which \mathbf{d}^o is the *observed data vector* which contains all of the $4N$ observations of f and
 126 its gradient, \mathbf{d} is the *predicted data vector* from Equation 9, and \mathbf{W} is a $4N \times 4N$ diagonal
 127 weight matrix. The first N terms of the diagonal of \mathbf{W} are the weights for the potential field
 128 observations and the following $3N$ terms are the weights of x-, y-, and z-derivatives of the
 129 potential field, in order.

130 The constrained problem in Equation 11 can be transformed into an unconstrained problem
 131 by using the Lagrangian

$$\mathcal{L}(\mathbf{p}, \mathbf{d}, \boldsymbol{\lambda}) = [\mathbf{d}^o - \mathbf{d}]^T \mathbf{W} [\mathbf{d}^o - \mathbf{d}] + 2\boldsymbol{\lambda}^T \mathbf{e} , \quad (12)$$

132 in which $\boldsymbol{\lambda}$ is an $N \times 1$ vector of Lagrange multipliers. The non-linear Lagrangian is minimised
 133 through Newton's method (Aster et al., 2018). We start with initial estimates \mathbf{p}_0 and \mathbf{d}_0 and
 134 then iteratively apply corrections $\Delta\mathbf{p}_k$ and $\Delta\mathbf{d}_k$ until convergence is achieved. To calculate
 135 the corrections, we introduce a new variable $\mathbf{u} = [\mathbf{d}^T \ \boldsymbol{\lambda}^T \ \mathbf{p}^T]^T$, expand the Lagrangian $\mathcal{L}(\mathbf{u})$
 136 (Equation 12) in a Taylor series around point \mathbf{u}_k , and disregard terms of order higher than two

$$\mathcal{L}(\mathbf{u}) \approx \Gamma(\mathbf{u}) = \mathcal{L}(\mathbf{u}_k) + \Delta\mathbf{u}_k^T \nabla \mathcal{L}(\mathbf{u}_k) + \frac{1}{2} \Delta\mathbf{u}_k^T \mathbf{H}_k \Delta\mathbf{u}_k , \quad (13)$$

137 in which ∇ is the gradient operator and \mathbf{H}_k is the Hessian matrix of \mathcal{L} evaluated at \mathbf{u}_k .

¹³⁸ Equation 13 is a quadratic function of $\Delta \mathbf{u}_k$ and we can obtain its minimum by taking its gradient
¹³⁹ and equating it to the null vector

$$\nabla \Gamma(\Delta \mathbf{u}_k) = \nabla \mathcal{L}(\mathbf{u}_k) + \mathbf{H}_k \Delta \mathbf{u}_k = \mathbf{0} , \quad (14)$$

$$\mathbf{H}_k \Delta \mathbf{u}_k = -\nabla \mathcal{L}(\mathbf{u}_k) .$$

¹⁴⁰ The equation above is the *system of normal equations*, which can also be written in terms of \mathbf{p} ,
¹⁴¹ $\boldsymbol{\lambda}$, and \mathbf{d}

$$\underbrace{\begin{bmatrix} \mathbf{H}_k^{dd} & \mathbf{H}_k^{d\lambda} & \mathbf{H}_k^{dp} \\ \mathbf{H}_k^{\lambda d} & \mathbf{H}_k^{\lambda\lambda} & \mathbf{H}_k^{\lambda p} \\ \mathbf{H}_k^{pd} & \mathbf{H}_k^{p\lambda} & \mathbf{H}_k^{pp} \end{bmatrix}}_{\text{Hessian of } \mathcal{L}} \underbrace{\begin{bmatrix} \Delta \mathbf{d}_k \\ \Delta \boldsymbol{\lambda}_k \\ \Delta \mathbf{p}_k \end{bmatrix}}_{\Delta \mathbf{u}_k} = -\underbrace{\begin{bmatrix} \nabla_d \mathcal{L}(\mathbf{p}_k, \mathbf{d}_k, \boldsymbol{\lambda}_k) \\ \nabla_\lambda \mathcal{L}(\mathbf{p}_k, \mathbf{d}_k, \boldsymbol{\lambda}_k) \\ \nabla_p \mathcal{L}(\mathbf{p}_k, \mathbf{d}_k, \boldsymbol{\lambda}_k) \end{bmatrix}}_{\text{gradient of } \mathcal{L}} , \quad (15)$$

¹⁴² in which ∇_α is the gradient operator with respect to variable α and $\mathbf{H}_k^{\alpha\beta}$ is the Hessian matrix
¹⁴³ of \mathcal{L} with respect to variables α and β , evaluated at \mathbf{u}_k . Since the order of derivation can be
¹⁴⁴ swapped in the Hessian matrices and the Hessian of \mathcal{L} is symmetric, the above equation can be
¹⁴⁵ simplified to

$$\begin{bmatrix} \mathbf{H}_k^{dd} & \mathbf{H}_k^{d\lambda} & \mathbf{H}_k^{dp} \\ \mathbf{H}_k^{d\lambda T} & \mathbf{H}_k^{\lambda\lambda} & \mathbf{H}_k^{\lambda p} \\ \mathbf{H}_k^{dp T} & \mathbf{H}_k^{\lambda p T} & \mathbf{H}_k^{pp} \end{bmatrix} \begin{bmatrix} \Delta \mathbf{d}_k \\ \Delta \boldsymbol{\lambda}_k \\ \Delta \mathbf{p}_k \end{bmatrix} = -\begin{bmatrix} \nabla_d \mathcal{L}(\mathbf{p}_k, \mathbf{d}_k, \boldsymbol{\lambda}_k) \\ \nabla_\lambda \mathcal{L}(\mathbf{p}_k, \mathbf{d}_k, \boldsymbol{\lambda}_k) \\ \nabla_p \mathcal{L}(\mathbf{p}_k, \mathbf{d}_k, \boldsymbol{\lambda}_k) \end{bmatrix} . \quad (16)$$

¹⁴⁶ Now, we must derive the three gradient vectors and six Hessian matrices in Equation 16. We
¹⁴⁷ will start with the gradient vectors.

$$\begin{aligned} \nabla_d \mathcal{L}(\mathbf{p}_k, \mathbf{d}_k, \boldsymbol{\lambda}_k) &= 2(-\mathbf{W}[\mathbf{d}^o - \mathbf{d}_k] + \mathbf{B}_k^T \boldsymbol{\lambda}_k) , \\ \nabla_\lambda \mathcal{L}(\mathbf{p}_k, \mathbf{d}_k, \boldsymbol{\lambda}_k) &= 2\mathbf{e}_k , \\ \nabla_p \mathcal{L}(\mathbf{p}_k, \mathbf{d}_k, \boldsymbol{\lambda}_k) &= 2\mathbf{A}_k^T \boldsymbol{\lambda}_k , \end{aligned} \quad (17)$$

¹⁴⁸ in which $\mathbf{e}_k = \mathbf{e}(\mathbf{p}_k, \mathbf{d}_k)$ (Equation 10), \mathbf{A}_k is the $N \times 4$ parameter Jacobian matrix of Euler's
¹⁴⁹ equation (Equation 5) evaluated on $(\mathbf{p}_k, \mathbf{d}_k)$, and \mathbf{B}_k is the $N \times 4N$ data Jacobian of Euler's
¹⁵⁰ equation, also evaluated on $(\mathbf{p}_k, \mathbf{d}_k)$. The data Jacobian \mathbf{B}_k contains the first derivatives of

₁₅₁ Euler's equation (Equation 1) with respect to the data vector \mathbf{d} (Equation 9). It is composed of
₁₅₂ four diagonal matrices

$$\mathbf{B}_k = \begin{bmatrix} \mathbf{B}_k^f & \mathbf{B}_k^x & \mathbf{B}_k^y & \mathbf{B}_k^z \end{bmatrix} . \quad (18)$$

₁₅₃ The diagonal elements of each of the four matrices are

$$B_{kii}^f = \eta , \quad B_{kii}^x = x_i - x_{ok} , \quad B_{kii}^y = y_i - y_{ok} , \quad B_{kii}^z = z_i - z_{ok} . \quad (19)$$

₁₅₄ The Hessian matrices are calculated using a Gauss-Newton approximation disregarding
₁₅₅ second-order derivatives. The six independent Hessians are given by

$$\begin{aligned} \mathbf{H}_k^{dd} &\approx 2\mathbf{W} , \quad \mathbf{H}_k^{\lambda\lambda} = \mathbf{0} , \quad \mathbf{H}_k^{pp} \approx \mathbf{0} , \\ \mathbf{H}_k^{d\lambda} &= 2\mathbf{B}^T , \quad \mathbf{H}_k^{\lambda p} = 2\mathbf{A} , \quad \mathbf{H}_k^{dp} \approx \mathbf{0} . \end{aligned} \quad (20)$$

₁₅₆ Substituting the gradients (Equation 17) and Hessians (Equation 20) into the system of normal
₁₅₇ equations of Newton's method (Equation 16) we arrive at

$$\begin{bmatrix} \mathbf{W} & \mathbf{B}_k^T & \mathbf{0} \\ \mathbf{B}_k & \mathbf{0} & \mathbf{A}_k \\ \mathbf{0} & \mathbf{A}_k^T & \mathbf{0} \end{bmatrix} \begin{bmatrix} \Delta\mathbf{d}_k \\ \Delta\boldsymbol{\lambda}_k \\ \Delta\mathbf{p}_k \end{bmatrix} = - \begin{bmatrix} -\mathbf{W}[\mathbf{d}^o - \mathbf{d}_k] + \mathbf{B}_k^T\boldsymbol{\lambda}_k \\ \mathbf{e}_k \\ \mathbf{A}_k^T\boldsymbol{\lambda}_k \end{bmatrix} . \quad (21)$$

₁₅₈ Since the data weight matrix \mathbf{W} is diagonal and invertible, we can use the following identity
₁₅₉ to eliminate one equation from the equation system above (Wells and Krakiwsky, 1971)

$$\begin{bmatrix} \mathbf{C} & \mathbf{D} \\ \mathbf{E} & \mathbf{F} \end{bmatrix} \begin{bmatrix} \mathbf{g} \\ \mathbf{h} \end{bmatrix} + \begin{bmatrix} \mathbf{t} \\ \mathbf{v} \end{bmatrix} = \begin{bmatrix} \mathbf{0} \\ \mathbf{0} \end{bmatrix} \Rightarrow [\mathbf{F} - \mathbf{E}\mathbf{C}^{-1}\mathbf{D}] \mathbf{h} + \mathbf{v} - \mathbf{E}\mathbf{C}^{-1}\mathbf{t} = \mathbf{0} . \quad (22)$$

₁₆₀ Applying the identity to Equation 21 with $\mathbf{g} = \Delta\mathbf{d}_k$ and $\mathbf{h} = [\Delta\boldsymbol{\lambda}_k \quad \Delta\mathbf{p}_k]^T$ leads to

$$\begin{bmatrix} -\mathbf{Q}_k & \mathbf{A}_k \\ \mathbf{A}_k^T & \mathbf{0} \end{bmatrix} \begin{bmatrix} \Delta\boldsymbol{\lambda}_k \\ \Delta\mathbf{p}_k \end{bmatrix} + \begin{bmatrix} \mathbf{e}_k + \mathbf{B}_k\mathbf{r}_k - \mathbf{Q}_k\boldsymbol{\lambda}_k \\ \mathbf{A}_k^T\boldsymbol{\lambda}_k \end{bmatrix} = \begin{bmatrix} \mathbf{0} \\ \mathbf{0} \end{bmatrix} . \quad (23)$$

161 in which $\mathbf{Q}_k = \mathbf{B}_k \mathbf{W}^{-1} \mathbf{B}_k^T$ and $\mathbf{r}_k = [\mathbf{d}^o - \mathbf{d}_k]$ is the residual vector. Applying the identity once
 162 more to the equation system above leads to a solution for the parameter correction vector

$$\hat{\Delta}\mathbf{p}_k = -[\mathbf{A}_k^T \mathbf{Q}_k^{-1} \mathbf{A}_k]^{-1} \mathbf{A}_k^T \mathbf{Q}_k^{-1} [\mathbf{B}_k \mathbf{r}_k + \mathbf{e}_k] . \quad (24)$$

163 We can obtain an expression for $\hat{\Delta}\boldsymbol{\lambda}_k$ as a function of $\hat{\Delta}\mathbf{p}_k$ from Equation 23, which results
 164 in

$$\hat{\Delta}\boldsymbol{\lambda}_k = \mathbf{Q}_k^{-1} [\mathbf{A}_k^T \hat{\Delta}\mathbf{p}_k + \mathbf{B}_k \mathbf{r}_k + \mathbf{e}_k] - \boldsymbol{\lambda}_k . \quad (25)$$

165 Finally, we can substitute the expression above into the first equation of the system of normal
 166 equations (Equation 21) to obtain the data correction as a function of $\hat{\Delta}\mathbf{p}_k$

$$\hat{\Delta}\mathbf{d}_k = \mathbf{r}_k - \mathbf{W}^{-1} \mathbf{B}_k^T \mathbf{Q}_k^{-1} [\mathbf{A}_k^T \hat{\Delta}\mathbf{p}_k + \mathbf{B}_k \mathbf{r}_k + \mathbf{e}_k] . \quad (26)$$

167 The covariance matrix of \mathbf{p} is used to rank and filter solutions during the moving window
 168 procedure. It can be estimated by propagating uncertainties from the observed data \mathbf{d}^o to
 169 the parameter correction vector (Equation 24) and, hence, to the parameter vector (Wells and
 170 Krakiwsky, 1971). The covariance matrix of the observed data is approximated by $\mathbf{C}_d = \hat{\sigma}_0^2 \mathbf{W}^{-1}$.
 171 Recalling that matrix \mathbf{Q} is diagonal, the parameter covariance matrix is estimated at the last
 172 iteration of the Gauss-Newton method (iteration L) as

$$\begin{aligned} \mathbf{C}_p &= [\mathbf{A}_L^T \mathbf{Q}_L^{-1} \mathbf{A}_L]^{-1} \mathbf{A}_L^T \mathbf{Q}_L^{-1} \mathbf{B}_L \mathbf{C}_d \mathbf{B}_L^T \mathbf{Q}_L^{-1} \mathbf{A}_L [\mathbf{A}_L^T \mathbf{Q}_L^{-1} \mathbf{A}_L]^{-1} , \\ &= \hat{\sigma}_0^2 [\mathbf{A}_L^T \mathbf{Q}_L^{-1} \mathbf{A}_L]^{-1} , \end{aligned} \quad (27)$$

173 in which $\hat{\sigma}_0^2 = \|\mathbf{d}^o - \mathbf{d}_L\|^2 / (4N - 4)$ is the reduced chi-squared statistic of the Euler inversion
 174 and an estimate of the variance factor of the observed data \mathbf{d}^o .

175 **2.3 Euler inversion: Practical implementation**

176 **2.3.1 Initial estimates and convergence**

177 Unlike a traditional Gauss-Newton inversion of a parametric model, the Euler inversion procedure
178 estimates corrections to both the parameter vector \mathbf{p} and the predicted data vector \mathbf{d} at each
179 iteration. Hence, the optimisation requires initial values for both the parameters and the
180 predicted data. The initial value of the parameters is taken as the solution of traditional Euler
181 deconvolution $\mathbf{p}_0 = [\mathbf{A}^T \mathbf{A}]^{-1} \mathbf{A}^T \mathbf{c}$ (Equation 6). The initial value for the predicted data should
182 be close to the observed data. We found that in practice a reasonably fast convergence is achieved
183 by assigning $\mathbf{d}_0 = 0.9 \mathbf{d}^o$.

184 Convergence of the solution cannot be directly evaluated by the value of the Lagrangian
185 (Equation 12) because values $\boldsymbol{\lambda}$ are not calculated. Instead, we specify a *merit function* \mathcal{M}
186 which combines the data misfit as well as the adherence to the constraints

$$\mathcal{M}_k(\mathbf{p}_k, \mathbf{d}_k) = \sqrt{\mathbf{r}_k^T \mathbf{W} \mathbf{r}_k} + \nu \sqrt{\mathbf{e}_k^T \mathbf{e}_k} . \quad (28)$$

187 in which $\sqrt{\mathbf{r}_k^T \mathbf{W} \mathbf{r}_k}$ is the *weighted root-mean-squared error* (WRMSE) and ν is a trade-off
188 parameter that balances fitting the data and strict adherence to the constraints. In practice, we
189 have found that a value of $\nu = 0.1$ works well in all of our synthetic data tests and our field data
190 application. The merit function is evaluated at every iteration. The non-linear optimisation
191 stops when a given maximum number of iterations is reached, the merit function increases, or
192 when the change in its value drops below a given threshold.

193 An outline of the entire Euler inversion procedure is given in Algorithm 1. Notice that
194 Equations 24 and 26 for calculating $\Delta\mathbf{p}_k$ and $\Delta\mathbf{d}_k$ do not depend on $\boldsymbol{\lambda}_k$ or $\Delta\boldsymbol{\lambda}_k$. Thus,
195 Equation 25 does not need to be calculated in practice.

196 **2.3.2 Structural index estimation**

197 An advantage of Euler inversion over Euler deconvolution is its ability to obtain predicted
198 values of the potential field and its gradient. In Section 3.2, we demonstrate that the *weighted*

Algorithm 1: The Euler inversion Gauss-Newton optimization method.

```
1 Set  $\mathbf{p}_0 = [\mathbf{A}^T \mathbf{A}]^{-1} \mathbf{A}^T \mathbf{c}$  and  $\mathbf{d}_0 = 0.9 \mathbf{d}^o$  ;
2 Evaluate  $\mathcal{M}_0(\mathbf{p}_0, \mathbf{d}_0)$  ;
3 for  $k = 0$  to  $L - 1$  do
4     Calculate the parameter correction  $\Delta\mathbf{p}_k$  using Equation 24 ;
5     Calculate the predicted data correction  $\Delta\mathbf{d}_k$  using Equation 26 ;
6     Update  $\mathbf{p}_{k+1} = \mathbf{p}_k + \Delta\mathbf{p}_k$  and  $\mathbf{d}_{k+1} = \mathbf{d}_k + \Delta\mathbf{d}_k$  ;
7     Evaluate  $\mathcal{M}_{k+1}(\mathbf{p}_{k+1}, \mathbf{d}_{k+1})$  ;
8     if  $\mathcal{M}_{k+1} > \mathcal{M}_k$  then
9         Undo the previous update of  $\mathbf{p}$  and  $\mathbf{d}$  ;
10        Exit ;
11    end if
12    if  $|\mathcal{M}_{k+1} - \mathcal{M}_k| / \mathcal{M}_k < \delta$  then
13        Exit ;
14    end if
15 end for
16 Calculate the  $\hat{\sigma}_0^2$  using the last residuals  $\mathbf{r}_L$  ;
17 Calculate  $\mathbf{C}_p$  using Equation 27 ;
```

¹⁹⁹ root-mean-squared error

$$\text{WRMSE} = \sqrt{[\mathbf{d}^o - \mathbf{d}_L]^T \mathbf{W} [\mathbf{d}^o - \mathbf{d}_L]}, \quad (29)$$

²⁰⁰ of the predicted data at the L -th iteration \mathbf{d}_L appears to be smallest when the correct structural
²⁰¹ index η is used. Given this observation, we can estimate the optimal value of η by running
²⁰² the Euler inversion in a given data window for different values of η and choosing the one that
²⁰³ produces the smallest WRMSE. This procedure is summarised in Algorithm 2.

Algorithm 2: Structural index estimation through Euler inversion.

```
1 for  $\eta = \eta_{min}$  to  $\eta_{max}$  do
2   Run Algorithm 1 to estimate  $\mathbf{p}_\eta$  and  $\mathbf{d}_\eta$  ;
3   Calculate the WRMSE( $\eta$ ) =  $\sqrt{[\mathbf{d}^o - \mathbf{d}_\eta]^T \mathbf{W} [\mathbf{d}^o - \mathbf{d}_\eta]}$  for the estimated  $\mathbf{d}_\eta$  ;
4 end for
5 Choose optimal  $\eta = \operatorname{argmin}_\eta \text{WRMSE}(\eta)$  and the corresponding  $\mathbf{p}_\eta$  and  $\mathbf{d}_\eta$  ;
```

204 **2.3.3 Moving window procedure**

205 For cases with multiple sources in a given dataset, we adopt a moving window procedure similar
206 to the classic Euler deconvolution. We divide the data region into M overlapping windows. For
207 each window, we run Algorithm 2 to obtain an estimate of the parameters and the structural
208 index η . This procedure leads to spurious solutions, much like standard Euler deconvolution,
209 in cases where there are no sources inside windows or when sources are heavily truncated. To
210 filter out spurious sources, we rank the solutions for each structural index separately by the
211 variance of the z_o estimate (from Equation 27) and keep only a given percentage of those with
212 the smallest variance. This procedure is summarised in Algorithm 3.

Algorithm 3: Moving window procedure for Euler inversion.

```
1 Divide the data region into  $M$  overlapping windows with a defined degree of overlap ;
2 Define a ratio  $0 < \gamma \leq 1$  of estimates to keep ;
3 for  $l = 1$  to  $M$  do
4   Run Algorithm 2 on the data from window  $l$  to estimate  $\mathbf{p}$ ,  $\mathbf{d}$ ,  $\mathbf{C}_p$ , and  $\eta$  ;
5 end for
6 for  $\eta = \eta_{min}$  to  $\eta_{max}$  do
7   Sort the  $M_\eta$  solutions which produced an estimated SI equal to  $\eta$  by the estimated
     variance of  $z_o$  in increasing order ;
8   Keep the first  $\gamma M_\eta$  solutions and discard the remainder ;
9 end for
```

213 3 Results

214 In this section, we demonstrate the effectiveness and limitations of the Euler inversion method by
215 applying it to a series of synthetic datasets and to real aeromagnetic data from Rio de Janeiro,
216 Brazil. The applications are organised as follows:

- 217 1. **Method demonstration:** This test uses a single data window and a single dipolar source.
218 Its aim is to demonstrate the convergence of the Euler inversion method and its ability
219 to correctly estimate the source position when the structural index is known, even in the
220 presence of random noise.
- 221 2. **Effect of structural index choice:** This test uses several different sources, each in a
222 separate data window, and runs the Euler inversion method on each with different values of
223 the structural index η . Its aim is to determine the effect of the choice of η on the estimated
224 coordinates and the weighted root-mean-squared error (Equation 28).
- 225 3. **Effect of random noise:** This test uses a single dipolar source and a single data window
226 with data contaminated with increasing levels of pseudo-random noise. Its aim is to
227 investigate the effect of random high-frequency noise on the Euler inversion estimated
228 source coordinates, base level, and structural index.
- 229 4. **Effect of interfering sources:** This test uses four different models of a dipolar source and
230 a single data window with an interfering dipolar source present in different locations and
231 depths. Its aim is to investigate the effect of interfering sources inside the data window on
232 the Euler inversion, Euler deconvolution, and finite-difference Euler deconvolution results.
- 233 5. **Moving window procedure with multiple sources:** This test combines several sources
234 and uses the moving window procedure from Algorithm 3. Its aim is to show how the
235 Euler inversion method behaves on a more complex dataset and provide a comparison with
236 standard Euler deconvolution and finite-difference Euler deconvolution.
- 237 6. **Aeromagnetic data from Rio de Janeiro, Brazil:** This test applies the Euler inversion

method to a real dataset which contains multiple sources. Its aim is to demonstrate the effectiveness of the method on a real dataset with realistic levels of noise, signal overlap, and geometry of sources.

The Python source code used to produce the results presented here, as well as extra explanation of the models and procedures, can be found in the supplementary information at <https://doi.org/10.6084/m9.figshare.26384140> (Uieda et al., 2024).

3.1 Method demonstration

The main goal of this synthetic data test is to demonstrate the general effectiveness of the Euler inversion method to estimate the position and base level of a single source. To this end, we created a model composed of a single dipole located at ($x_o = 15\,000\text{ m}$, $y_o = 12\,000\text{ m}$, $z_o = -3000\text{ m}$) with a dipole moment magnitude of $5 \times 10^{11}\text{ A m}^{-1}$, inclination of -30° , and declination of 15° . The reference field direction was the same as the dipole moment direction. The synthetic total-field magnetic anomaly data was calculated on a regular grid with point spacing of 300 m at a height of 800 m. To the data, we added a base level of 100 nT and pseudo-random Gaussian noise with 0 nT mean and 10 nT standard deviation. The eastward and northward derivatives of the total-field anomaly grid were calculated with a central-difference scheme. The upward derivative was calculated by Fast Fourier Transform (FFT). The synthetic anomaly and its three derivatives are shown in Figures 1a-d.

The Euler inversion method described in Algorithm 1 was applied to the synthetic data. We chose a fixed structural index of $\eta = 3$, which is the correct index for a magnetic dipole. For data weights, we used 1 for the total-field anomaly, 0.1 for the east-derivative, 0.1 for the north-derivative, and 0.025 for the upward-derivative. These weights were chosen to counteract the increased effect of noise on the derivatives, particularly the upward derivative which was calculated through FFT. Figures 1e-h show the inversion residuals after convergence was achieved ($L = 6$ iterations) for the total-field anomaly and its eastward, northward, and upward derivatives, respectively. Also shown are the true source location, the initial source location (the Euler deconvolution result), and the predicted source location from Euler inversion. The final Euler

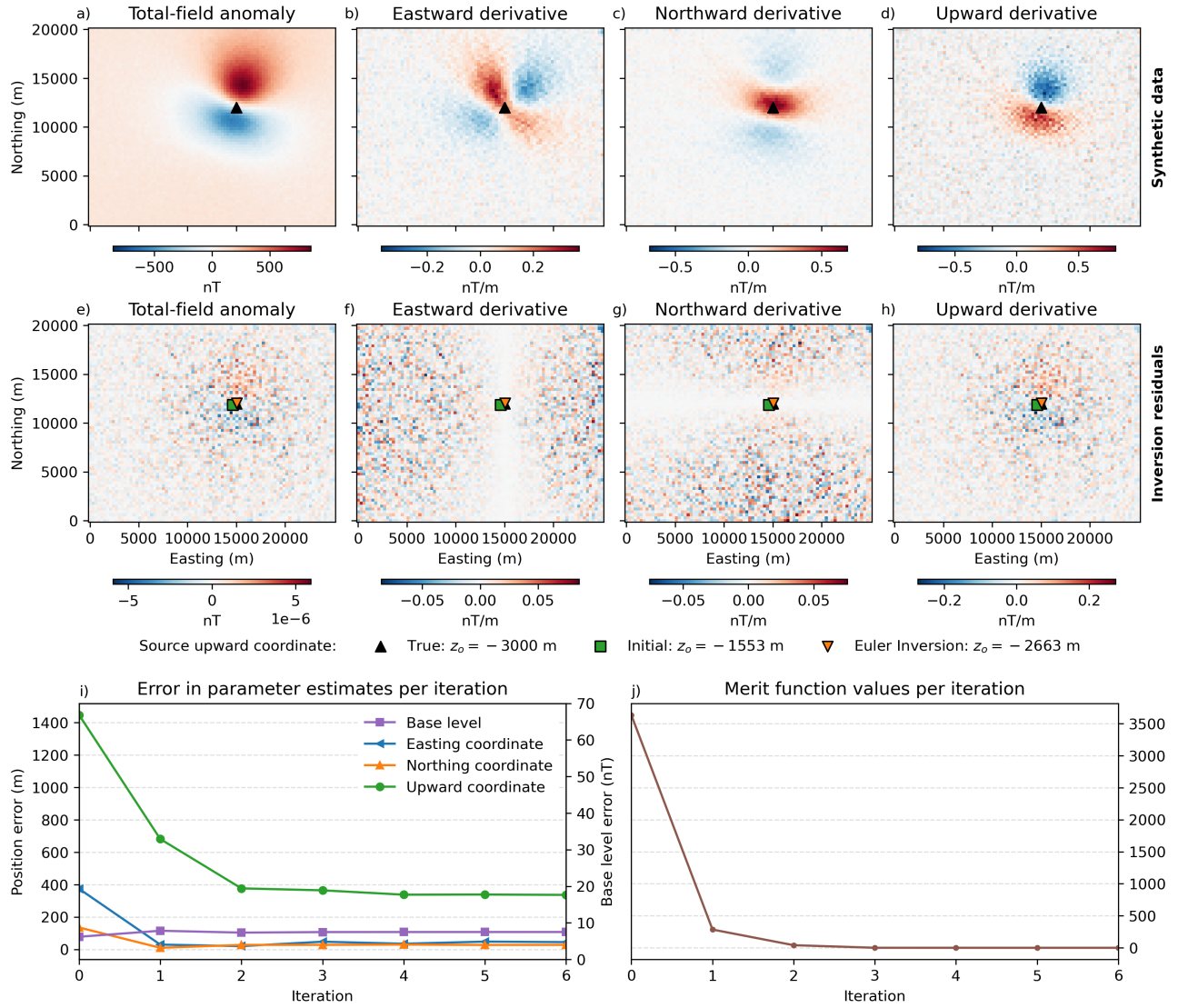


Figure 1: Data and results from the synthetic data test to demonstrate the performance of the method on a single target. a-d) The noise-corrupted synthetic total-field anomaly and its eastward, northward, and upward derivatives, respectively. The position of the dipolar source is marked by the black triangle. e-h) The Euler inversion residuals (observed data minus predicted data) for the total-field anomaly and its easting, northing, and upward derivatives, respectively. The black triangle shows the true location of the source, the green square shows the location estimated by Euler deconvolution, and the orange triangle shows the location estimated by Euler inversion. i) The error in the estimate of the easting (blue line), northing (orange line), and upward (green line) coordinates of the source and the base level (purple line) as a function of the Gauss-Newton iteration (Algorithm 1). j) The value of the merit function \mathcal{M} (Equation 28) per Gauss-Newton iteration.

inversion prediction of the source location was $(x_o = 15\,045 \text{ m}, y_o = 12\,028 \text{ m}, z_o = -2663 \text{ m})$ and the estimated base level was $b = 93 \text{ nT}$, which is an improvement on the estimated values by Euler deconvolution (Figure 1).

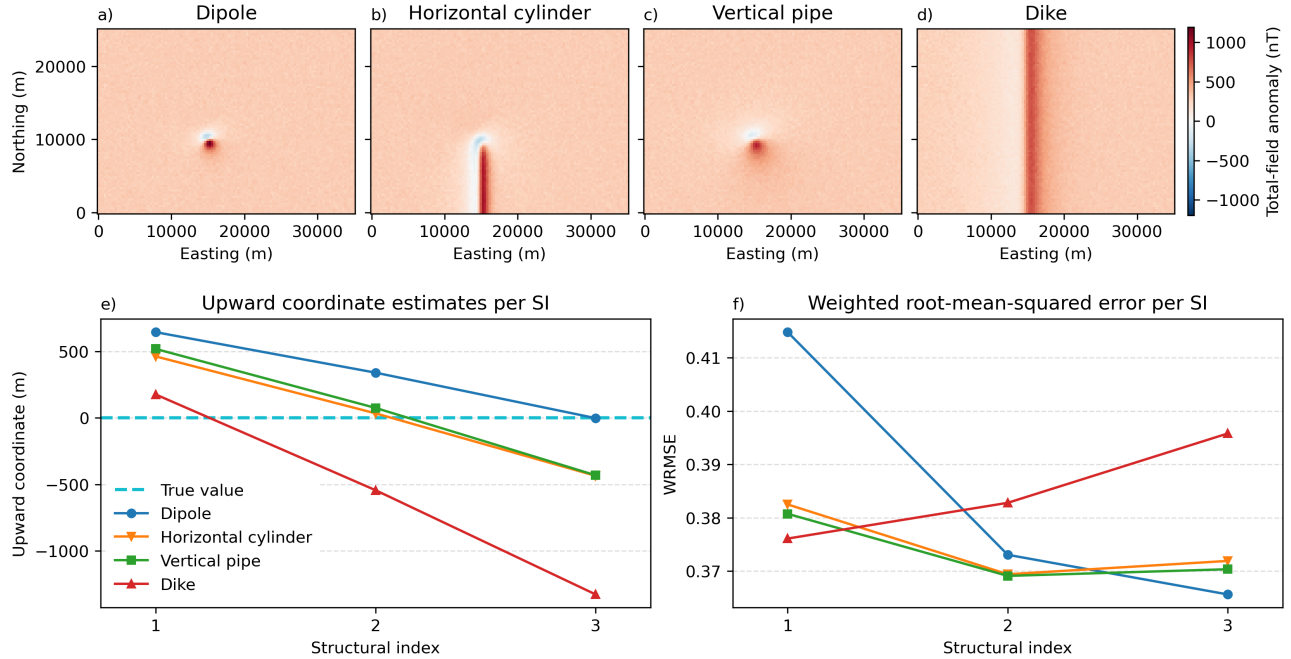


Figure 2: Data and results from the synthetic data test using different values of structural index η for different source types. a-d) Noise-corrupted total-field magnetic anomaly data caused by a dipole ($\eta = 3$), a horizontal cylinder ($\eta = 2$), a vertical pipe ($\eta = 2$), and a vertical North-South dyke ($\eta = 1$), respectively. e) Estimate of the upward source coordinate z_o as a function of structural index for the dipole (blue line), horizontal cylinder (orange line), vertical pipe (green line), and dyke (red line). The true upward coordinate of the sources ($z_o = 0$ m) is marked by the blue dashed line. Note that the z_o estimate is closest to the true value when the correct structural index for each source type is used. f) The weighted root-mean-squared error (WRMSE; Equation 29) as a function of structural index for the dipole (blue line), horizontal cylinder (orange line), vertical pipe (green line), and dyke (red line). The WRMSE is minimum for each source type when the correct structural index is used.

268 The convergence of the solution is shown in Figures 1i-j. The error in the estimated source
 269 coordinates and base level are shown in Figure 1i. The error in the x_o (easting) and y_o (northing)
 270 coordinates, as well as the base level, do not vary greatly from the initial solution. However, the
 271 error in the z_o (upward) coordinate drops from over 1400 m to less than 400 m in two iterations.
 272 The merit function (Equation 28) also drops sharply in value by two iterations, as can be seen
 273 in Figure 1j, confirming the rapid convergence of the Euler inversion method.

²⁷⁴ **3.2 Effect of structural index choice**

²⁷⁵ In this synthetic data test, we created datasets using four different models: a dipole, a horizontal
²⁷⁶ cylinder composed of a right-rectangular prism stretched in the southward direction, a vertical
²⁷⁷ pipe composed of a right-rectangular prism stretched in the downward direction, and a vertical
²⁷⁸ dyke composed of a right-rectangular prism stretched in the southward, northward, and downward
²⁷⁹ directions. All models share the same true location of ($x_o = 15\,000\text{ m}$, $y_o = 10\,000\text{ m}$, $z_o = 0\text{ m}$),
²⁸⁰ base level of 300 nT , and induced magnetisation with inclination of 35° and declination of
²⁸¹ -20° . The data were generated on a regular grid with spacing of 300 m , height of 1000 m , and
²⁸² contaminated with pseudo-random Gaussian noise with 0 nT mean and 15 nT standard deviation.
²⁸³ Figures 2a-d show the synthetic noise-corrupted total-field anomaly data.

²⁸⁴ We ran the Euler inversion method on each data grid three times, each time changing
²⁸⁵ the structural index between one, two, and three. Figure 2e shows the upward coordinate z_o
²⁸⁶ estimated for each of the four models as a function of the structural index η . The Euler inversion
²⁸⁷ estimated z_o correlates with η , with larger values of the structural index leading to deeper source
²⁸⁸ estimates. Values closest to the true $z_o = 0\text{ m}$ are achieved when the correct structural index is
²⁸⁹ used ($\eta = 1$ for the dyke, $\eta = 2$ for the cylinder and pipe, and $\eta = 3$ for the dipole). Figure 2f
²⁹⁰ shows the weighted root-mean-squared error (WRMSE; Equation 29) at the final iteration of
²⁹¹ the Euler inversion method for all four models as a function of structural index. The WRMSE is
²⁹² a measure of goodness-of-fit between the predicted total-field anomaly and its three derivatives
²⁹³ and their observed counterparts. The WRMSE is minimum for all four models when the correct
²⁹⁴ structural index is used.

²⁹⁵ **3.3 Effect of random noise**

²⁹⁶ We conducted another experiment to determine the effect of random high-frequency noise on
²⁹⁷ the Euler inversion estimates. To this end, we created synthetic data from a dipole model
²⁹⁸ located at ($x_o = 15\,000\text{ m}$, $y_o = 11\,000\text{ m}$, $z_o = -5000\text{ m}$) and with a dipole moment magnitude
²⁹⁹ of $2 \times 10^{12}\text{ A m}^{-1}$, inclination of -30° , and declination of 15° . The total-field anomaly data

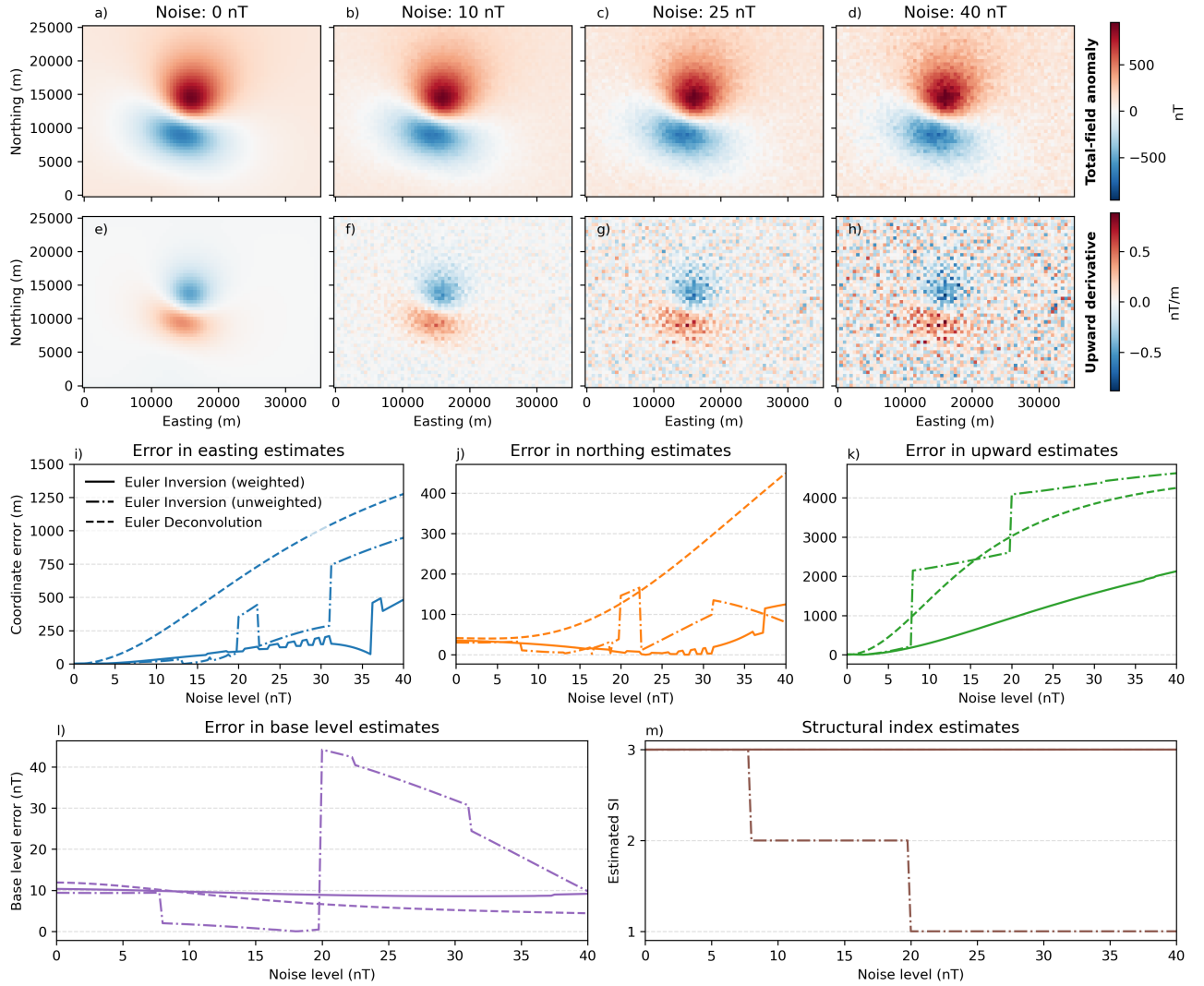


Figure 3: Data and results from the synthetic data test used to investigate the effect of high-frequency noise on the Euler inversion results. a-d) Noise-corrupted total-field magnetic anomaly of a dipolar source for noise levels 0, 10, 25, and 40 nT. e-h) The upward derivative of the data in a-d, calculated by FFT. i-k) Error in the estimated easting, northing, and upward coordinates, respectively. l) Error in the estimated base level. m) The estimated structural index η using Algorithm 2. The lines in i-m are the results for Euler deconvolution (dashed line), Euler inversion without data weights (dashed-dotted line), and Euler inversion with weights (solid line) 1 for the total-field anomaly, 0.1 for the eastward derivative, 0.1 for the northward derivative, and 0.025 for the upward derivative.

were generated on a regular grid with a spacing of 500 m and a constant height of 800 m. The reference field direction was the same as the dipole moment direction. A base level of 100 nT was added to the data. We generated different datasets by adding pseudo-random Gaussian noise with 0 nT mean and standard deviations varying from 0 nT to 40 nT with a step of 0.2 nT. Figures 3a-d show the synthetic data for noise levels 0, 10, 25, and 40 nT, while Figures 3e-h

305 show the upward derivative calculated from the total-field anomaly through FFT.

306 On each dataset, we ran Euler deconvolution (Equation 6), Euler inversion with unit weights,
307 and Euler inversion with weights 1 for the total-field anomaly, 0.1 for the eastward derivative,
308 0.1 for the northward derivative, and 0.025 for the upward derivative. Both Euler inversion
309 runs used the structural index estimation procedure (Algorithm 2). Figures 2i-l show the
310 error in the estimated easting, northing, and upward coordinates as well as the base level for
311 each of the methods as a function of noise level. The error in each of three coordinates raises
312 sharply with noise level for Euler deconvolution, particularly for the upward z_o coordinate.
313 The unweighted Euler inversion results vary less regularly but the present errors are just as
314 large as Euler deconvolution for the upward coordinate. However, the weighted Euler inversion
315 presented overall smaller errors and a slower growth curve for the upward coordinate error than
316 the other two methods. The base level error is nearly constant at approximately 10 nT for
317 Euler deconvolution and the weighted Euler inversion, but varies to as much as 40 nT for the
318 unweighted Euler inversion.

319 Figure 3m shows the estimated structural index η for the weighted and unweighted Euler
320 inversion as a function of noise level. The unweighted Euler inversion estimated the wrong
321 structural index $\eta = 2$ from approximately noise level 7 nT and $\eta = 1$ from approximately noise
322 level 20 nT. These jumps in the estimated structural index appear to correlate with jumps in
323 the base level and z_o coordinate errors. The weighted Euler inversion was able to estimate the
324 correct structural index ($\eta = 3$) for all noise levels tested.

325 3.4 Effect of interfering sources

326 Another common issue encountered during the application of Euler-based methods is the presence
327 of interfering sources within the data window. To test this effect on Euler inversion, we create
328 four different synthetic total-field anomaly datasets. All contain a main dipole located at
329 ($x_o = 13\,000$ m, $y_o = 11\,000$ m, $z_o = -4000$ m) with a dipole moment amplitude of 1×10^{12} A m⁻¹,
330 inclination of -30° , and declination of 15° . The reference field direction was the same as the
331 dipole moment direction. Each of the four models also contain a second dipolar source, simulating

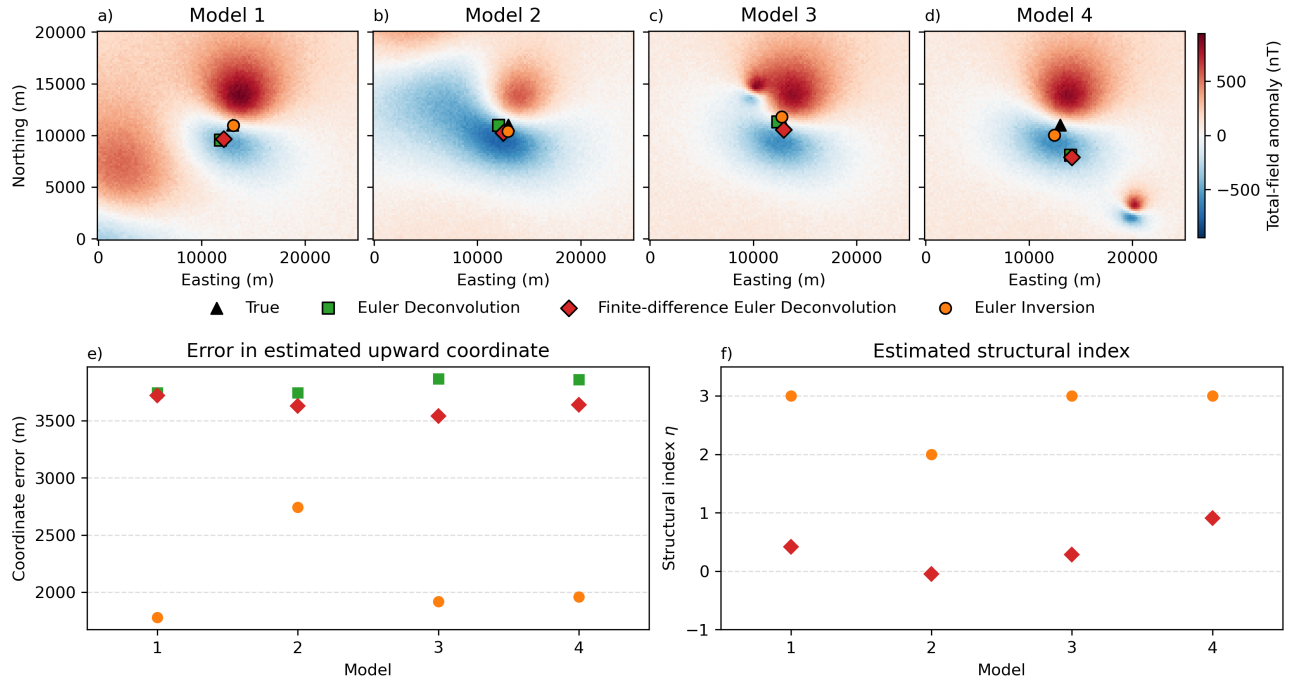


Figure 4: Data and results from the synthetic data test used to investigate the effect of interfering sources inside the data window on the Euler inversion results. a-d) Noise-corrupted total-field magnetic anomaly for four models, each of which include the same central dipole but different interfering sources in the form of another dipolar source. Also plotted are the estimated positions from Euler deconvolution, finite-difference Euler deconvolution, and Euler inversion. e) The error in the estimated upward coordinate of the source z_o for each of the Euler methods as a function of the model number. f) The estimated structural index η for Euler inversion and finite-difference Euler deconvolution as a function of the model number. The true source location is represented by a black triangle, the Euler deconvolution result by a green square, the finite-difference Euler deconvolution result by a red diamond, and the Euler inversion result by an orange circle.

an interfering source in the data window, that is located at different places and depths relative to the main dipole. The total-field anomaly data were generated on regular grids with a spacing of 200 m and at a constant height of 800 m. We added to all datasets a base level of 100 nT and pseudo-random Gaussian noise with 0 nT mean and 20 nT standard deviation. Figures 4a-d show the noise-corrupted total-field anomaly for each of the models.

On each dataset we, ran Euler deconvolution (Equation 6 with structural index $\eta = 3$), the finite-difference Euler deconvolution method of Gerovska et al. (2005), and Euler inversion with the structural index estimation (Algorithm 2) and data weights of 1 for the total-field anomaly, 0.1 for the eastward derivative, 0.1 for the northward derivative, and 0.025 for the upward

derivative. The estimated easting and northing coordinates are shown in Figures 4a-d. For models 2 and 3, all three methods performed similarly in estimating the horizontal coordinates of the true source. For models 1 and 4, the Euler deconvolution and finite-difference Euler deconvolution results are comparable, whilst the Euler inversion results are closer to the true source location. Figure 4e shows the error in the estimated upward coordinate for all three methods and four models. The Euler inversion errors are consistently lower than those of both Euler deconvolution methods. With the exception of model 2, the Euler inversion error on the upward coordinate are approximately half those of the Euler deconvolution methods. Figure 4f shows the estimated structural index for finite-difference Euler deconvolution and Euler inversion. The finite-difference Euler deconvolution method consistently estimated values lower than $\eta = 1$. With the exception of model 2, Euler inversion was able to estimate the correct structural index ($\eta = 3$) for all other models.

3.5 Moving window procedure with multiple sources

To simulate a more realistic dataset, we created a model composed of 10 sources combining dipoles at various locations and depths and vertical dykes at various orientations. All sources had induced magnetisation in the direction of the regional field with a inclination of -30° and declination of -20° . The total-field anomaly of the model was calculated on a regular grid with a spacing of 500 m and at a constant height of 1000 m. We added to the data a base level of 1000 nT, pseudo-random Gaussian noise with 0 nT and 50 nT standard deviation, and a regional field composed of a first-degree polynomial with angular coefficients of 0.02 nT m^{-1} in the eastward and -0.03 nT m^{-1} in the northward directions. The noise-corrupted total-field anomaly data are shown in Figure 5a.

To the dataset, we applied the moving window Euler inversion method (Algorithm 3), the finite-difference Euler deconvolution method of Gerovska et al. (2005), and standard Euler deconvolution (using structural indices 1, 2, and 3). Euler inversion was performed with data weights of 1 for the total-field anomaly, 0.1 for the eastward derivative, 0.1 for the northward derivative, and 0.025 for the upward derivative. All three methods used the same moving window

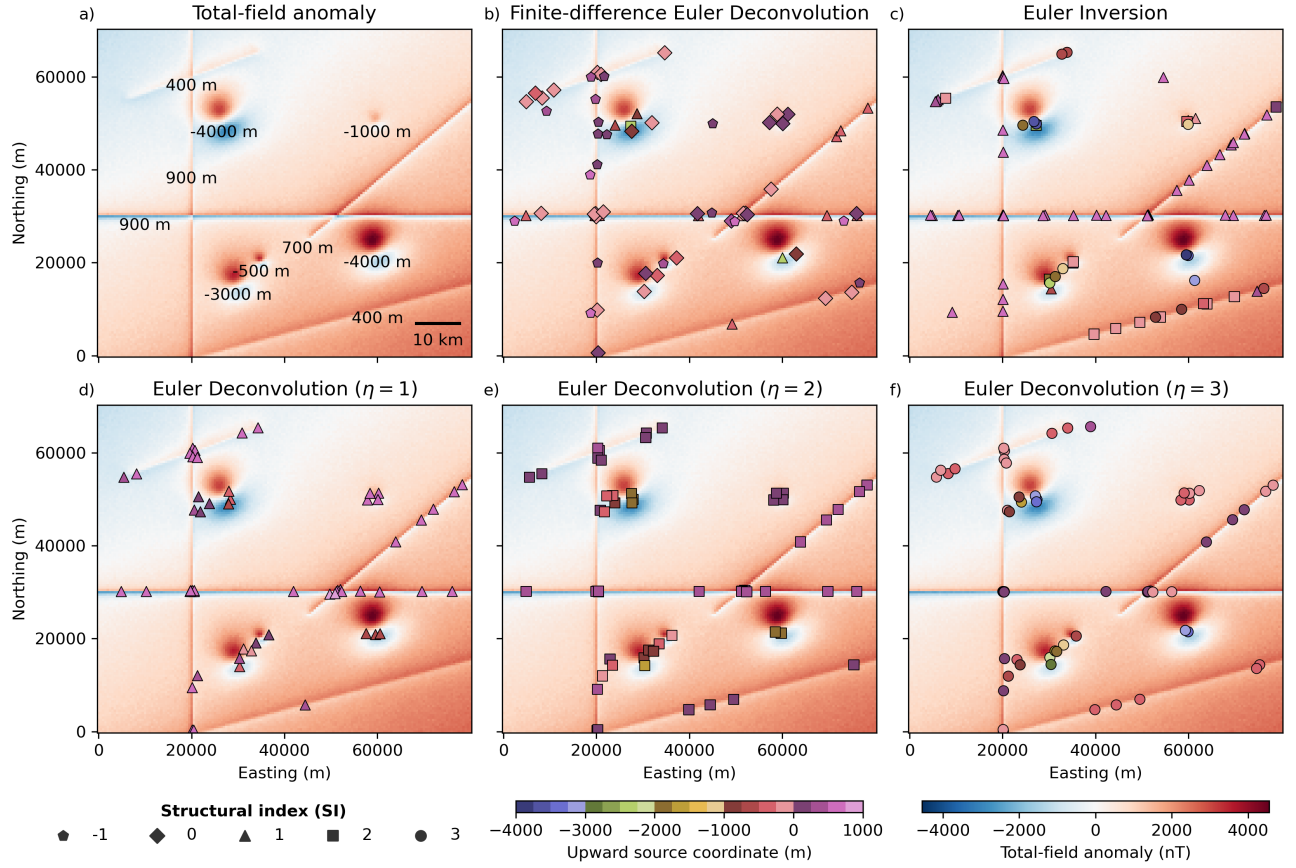


Figure 5: Data and results from the synthetic data test using the moving window scheme (Algorithm 3). a) Noise-corrupted total-field magnetic anomaly generated from 10 sources with overlapping signals, including dykes and dipoles. The true upward coordinate z_o of each source is shown next to their respective anomalies. b-f) The estimated source locations from finite-difference Euler deconvolution, Euler inversion, Euler deconvolution ($\eta = 1$), Euler deconvolution ($\eta = 2$), and Euler deconvolution ($\eta = 3$), respectively. The total-field anomaly is shown in the background for reference. The structural index of the solutions are represented by pentagons ($\eta = -1$), diamonds ($\eta = 0$), triangles ($\eta = 1$), squares ($\eta = 2$), and circles ($\eta = 3$). For finite-difference Euler deconvolution (b), the structural index symbol is that of the closest integer to the estimated value. The color of each symbol represents the estimated upward coordinate z_o . The window size used was 10 000 m and the step between windows was 5000 m.

procedure described in Algorithm 3 for the sake of comparison. The windows had a size of 10 000 m and were moved by 5000 m at a time. The ratio of estimates kept to form the final solution was $\gamma = 0.3$ for Euler deconvolution, $\gamma = 0.35$ for finite-difference Euler deconvolution, and $\gamma = 0.25$ for Euler inversion.

Figures 5b-f show the estimated source positions and structural indices for finite-difference Euler deconvolution, Euler inversion, and Euler deconvolution with structural indices 1, 2, and

3, respectively. The finite-difference method estimates a non-integer structural index, as a result
374 Figure 5b shows the closest integer value to the actual estimated η . The finite-difference Euler
375 deconvolution method underestimates the structural indices of all sources and, therefore, also
376 underestimates their depths. The finite-difference method solutions are also more scattered than
377 their Euler deconvolution and Euler inversion counterparts. The Euler deconvolution results
378 are closer to the correct depths when the correct structural index is used. They present larger
379 dispersion than Euler inversion in areas where the signals of multiple sources overlap. With
380 the exception of the deeper dykes in the northwest and southeast and the small dipole with
381 $z_o = -500$ m, Euler inversion is able to estimate the correct structural index for most sources.
382 The upward coordinate estimates for Euler inversion are also closer than Euler deconvolution
383 to their true values when the correct structural index was estimated. Euler inversion notably
384 estimates an incorrect η and z_o for smaller sources when there is a large amount of interference
385 in the anomalies and for dykes that are deeper and produce a smoother signal.

387 3.6 Aeromagnetic data from Rio de Janeiro

388 The geology of Rio de Janeiro state (Southeastern Brazil) consists primarily of high-grade
389 metamorphic rocks and granitoid magmatism related to the Ribeira Belt (RB) ([Heilbron et al.,
390 2020](#)). Figure 6a shows a simplified geologic map of the area, which was modified from [Heilbron
391 et al. \(2016\)](#) and [Dantas et al. \(2017\)](#). The Ribeira Belt is traditionally interpreted as a thrust belt
392 formed by diachronous collisions mainly between the São Francisco and Congo paleocontinents
393 ([Heilbron et al., 2008; Trouw et al., 2000](#)) or by an intracontinental orogeny (e.g. [Meira et al.,
394 2019, 2015](#)), during the Brasiliano orogeny. This process culminated in an orogen-parallel,
395 steep strike-slip shear system ([Egydio-Silva et al., 2005](#)), which deformed the Paleoproterozoic
396 basement rocks and reworked the Meso- to Neoproterozoic metasedimentary units (for example,
397 the Italva and São Fidelis groups) and syn-orogenic granitoid plutons (for example, the Rio
398 Negro complex) which formed during the orogeny ([Heilbron and Machado, 2003; Heilbron et al.,
399 2020](#)). These tectonic events imprinted a distinct NE-ENE-trending structural pattern onto
400 these rocks.

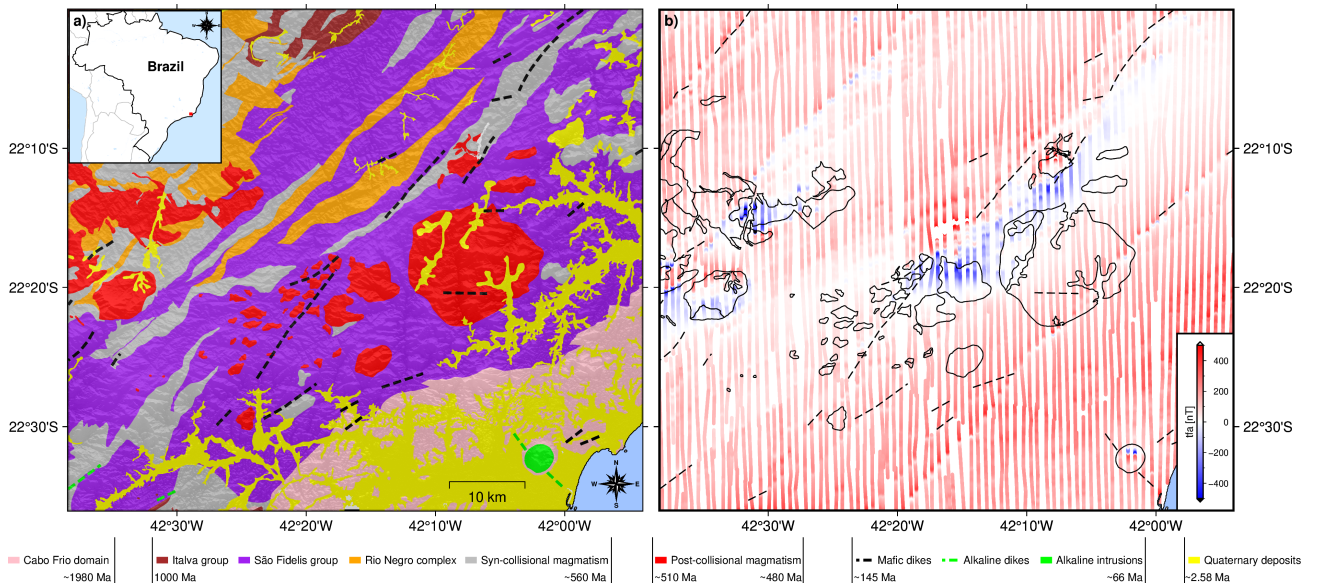


Figure 6: Geologic map and observed total-field magnetic anomaly data from the west of the state of Rio de Janeiro, Brazil. a) Simplified geologic map showing the main groups and dykes that outcrop in the region. In pink is the Cabo Frio domain, dark red is the Italva group, purple is the São Fidelis group, orange is the Rio Negro complex, gray is the syn-collisional magmatism, red is the post-collisional magmatism, green are alkaline intrusions, yellow are the Quaternary deposits, and the dashed lines are mafic and alkaline dykes. b) The aeromagnetic flight-line data, overlaid by the outlines of the post-collisional magmatism and alkaline intrusions (solid black lines) and dykes (dashed lines). The geologic map was modified from Heilbron et al. (2016) and Dantas et al. (2017).

401 The late Neoproterozoic to Cambrian period witnessed post-orogenic magmatism (*e.g.*,
 402 Valeriano et al., 2011), marking the final stages of the West Gondwana amalgamation. After
 403 this, the region remained tectonically quiescent until the Lower Cretaceous, when reactivation
 404 occurred with the emplacement of the NE-trending Serra do Mar mafic dyke swarm, preceding
 405 the break-up of West Gondwana and the opening of the South Atlantic Ocean (Almeida et al.,
 406 2013). Lastly, thermal anomalies in the region during the Upper Cretaceous to Paleocene period
 407 led to the emplacement of alkaline complexes and dykes (Thompson et al., 1998). The geological
 408 complexity of the Ribeira Belt, marked by the interplay of diverse tectonic regimes and magmatic
 409 events (Figure 6a), makes the Rio de Janeiro region an ideal test case for Euler inversion.

410 We used aeromagnetic data from the state of Rio de Janeiro which are distributed by the
 411 Serviço Geológico do Brasil (<https://geosgb.sgb.gov.br>). The data were collected in two
 412 phases: Subarea 1 was surveyed between March 25 and May 27, 1978, using an Islander aircraft

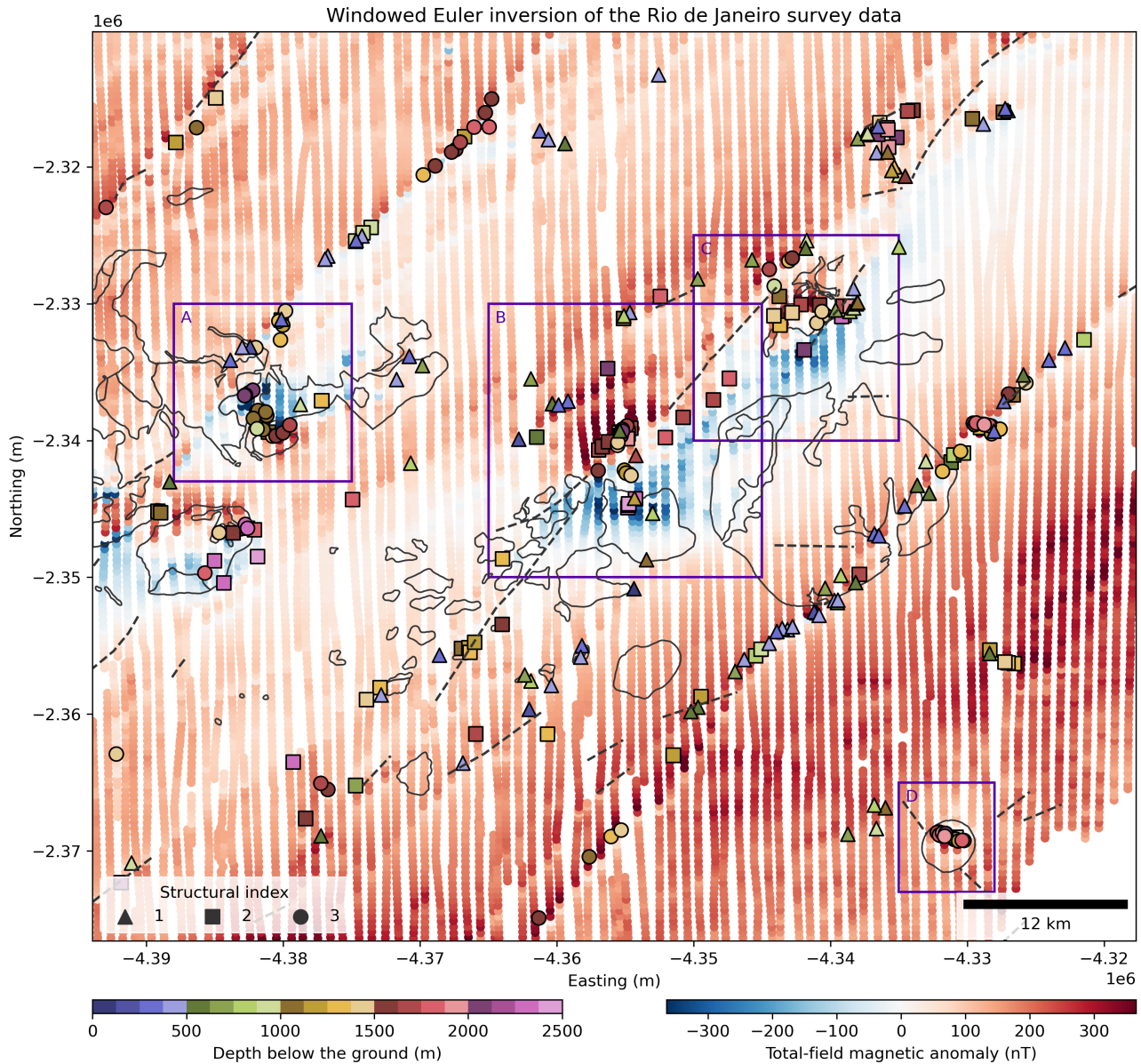


Figure 7: Results of applying Euler inversion with a window size of 12 000 m and a window step of 2400 m to the aeromagnetic data from Rio de Janeiro, Brazil. Estimated source locations and structural indices obtained from Euler inversion are shown as triangles ($\eta = 1$), squares ($\eta = 2$), and circles ($\eta = 3$). The colour of each symbol represents the estimated depth below the surface of the Earth (topography). Also shown are the total-field anomaly flight-line data, the contours of the post-collisional magmatism and alkaline intrusions (solid black lines) and dykes (dashed lines). The purple squares highlight the A, B, C, and D anomalies that are discussed in the text.

413 (PT-KRP), while Subarea 2 was surveyed between April 6 and July 19, 1978, using a Bandeirante
 414 aircraft (PT-GKJ), both funded by the Brazilian government. As shown in Figure 6b, the survey
 415 followed a pattern of north-south flight lines spaced approximately 1 km apart, with east-west tie

416 lines. Data were recorded at 100-meter intervals using a Geometrics G-803 magnetometer. Some
417 of the notable features of the data are the NE-SW linear features (interpreted here as dykes),
418 which coincide with known dyke outcrops, and complex dipolar anomalies which coincide with
419 some of the post-collisional magmatism and alkaline intrusions. A subset of 50 882 data points
420 were used in our analysis.

421 The data were not interpolated on a regular grid to avoid any smoothing effects that the
422 interpolation might have on the linear features. This could result in an over-estimation of their
423 depth, as discussed in Section 3.5. Instead, we used the gradient-boosted equivalent sources
424 method of Soler and Uieda (2021) to fit a model to the observed line data. We then used
425 the model to make predictions of the three spatial derivatives at the original measurement
426 locations by a central-difference method with a coordinate shift of 1 m. Further details about
427 the data processing can be found in the source code archive that accompanies this article
428 <https://doi.org/10.6084/m9.figshare.26384140> (Uieda et al., 2024).

429 We performed the moving-window Euler inversion (Algorithm 3) on the observed total-field
430 anomaly line data using windows of size of 12 000 m which were moved 2400 m at a time. The
431 proportion of solutions kept was $\gamma = 0.15$. The inversion was performed with data weights of 1
432 for the total-field anomaly, 0.1 for the eastward derivative, 0.1 for the northward derivative, and
433 0.05 for the upward derivative. To aid in the geological interpretation of the results, we converted
434 the estimated upward source coordinates z_o to depths below the surface of the Earth. We did so
435 by subtracting the estimated z_o from the interpolated topographic height of the Shuttle Radar
436 Topography Mission (SRTM; Earth Resources Observation And Science (EROS) Center, 2017).
437 The estimated positions and structural indices are shown in Figure 7.

438 The estimated source positions shown in Figure 7 highlight the NE-SW lineaments as well as
439 some of the more dipolar anomalies. The lineaments are estimated with a mix of $\eta = 1$, $\eta = 2$,
440 and $\eta = 3$. The southernmost lineament is mostly estimated with $\eta = 1$ and depths suggesting
441 that it does not outcrop in its southernmost parts (depths of 400 m to 600 m), which is consistent
442 with the geologic information in Figure 6a. The southernmost part of this lineament, in particular,
443 has an estimated $\eta = 3$, which is known to happen for deeper dykes in our synthetic data tests

(Section 3.5). Conversely, the northernmost part of the lineament has a larger prevalence of $\eta = 1$ with shallower depths which coincide with a known dyke outcrop. Other known dyke outcrops coincide with estimated sources with $\eta = 1$, however their depths range from 100 m to 300 m. This may be caused by an excess of smoothing in the vertical derivative or effects of noise in the estimated coordinates. The lineaments in the northwestern part of the region are also highlighted by estimated sources. However, their structural indices are a mix of $\eta = 2$ and $\eta = 3$, suggesting deeper sources. This is inline with the geologic information, which includes no outcrops of linear structures in the area.

The dipolar anomalies are associated with post-collisional and alkaline intrusions, many of which are also cut by known outcropping dykes or have known dykes with magnetic signals that significantly overlap with the dipolar anomalies. The Euler inversion estimated structural indices for them range from $\eta = 2$ to $\eta = 3$. We have highlighted four dipolar anomalies, marked as A, B, C, and D in Figure 7, to aid in our discussion.

• **Anomaly A:** Has a reversed polarity and linear feature to its north that is not associated with any known dyke outcrop. The linear feature is highlighted by Euler inversion estimates with $\eta = 1$ and depth of 300 m to 400 m, which can be interpreted as a non-outcropping dyke. The dipolar anomaly itself has Euler inversion solutions with $\eta = 3$ and depth of 1000 m to 2000 m. The solutions in the centre of the anomaly present a shallower depth than the solutions to the north and south of the anomaly centre. From the results on synthetic data in Section 3.5, we can interpret the depth range to be caused by the moving window procedure and the effect of interfering sources. The depth to the centre of the anomaly source is likely close to 1000 m.

• **Anomaly B:** The dipolar anomaly is likely associated with a non-outcropping portion of the post-collisional magmatism. The anomaly is cut by several NE-SW linear features, some of which overlap with known dyke outcrops. The linear feature to the north is associated with Euler inversion results with $\eta = 1$ and depths ranging from 300 m to 600 m, suggesting a non-outcropping dyke. At the centre of the anomaly are Euler inversion estimates with $\eta = 3$ and depth estimate of approximately 1400 m. The Euler inversion

472 solutions surrounding these central solutions are likely caused by interference from other
473 sources.

- 474 • **Anomaly C:** A dipolar anomaly associated with an outcropping portion of the post-
475 collisional magmatism. There is a known outcropping dyke to the south of the anomaly,
476 which is associated with Euler inversion estimates with $\eta = 1$ and depths ranging from
477 500 m to 1000 m. These depth estimates are likely overestimated because of the interference
478 of the dipolar anomaly. The main anomaly has Euler inversion solutions with $\eta = 2$ and
479 $\eta = 3$ and depths varying from 1400 m to 1800 m. There is no clear indication of which of
480 these estimates is more reliable.
- 481 • **Anomaly D:** A small dipolar anomaly associated with an outcropping alkaline intrusion.
482 The Euler inversion estimates have $\eta = 3$ and depths 1700 m to 2000 m. There are known
483 outcropping dykes around the main intrusion but they have no discernible magnetic
484 anomalies and no Euler inversion solutions associated with them.

485 Overall, the Euler inversion solutions in Figure 7 are consistent with the known geology in
486 Figure 6a. The main linear features are mostly associated with Euler inversion estimates with
487 $\eta = 1$ and shallow depths, particularly where known dyke outcrops are located. Deeper linear
488 features are estimated with $\eta = 2$ and $\eta = 3$, which is consistent with the synthetic data results
489 (Section 3.5). The dipolar anomalies have consistent Euler inversion estimates with $\eta = 3$ when
490 they are well isolated from interfering sources. Otherwise, they are estimated with a mix of
491 structural indices and depths, as was demonstrated in Section 3.5.

492 4 Conclusion

493 Euler deconvolution is a widely used method for locating the sources of potential-field data, but
494 under-performs in real-world scenarios due to its dependence on the chosen value of the structural
495 index η and its sensitivity to high-frequency noise and signal overlap. We have developed a new
496 method to solve Euler's homogeneity equation for the source position, base level, and integer
497 structural index, which we call *Euler inversion*. Unlike Euler deconvolution, Euler inversion is

498 also able to estimate the predicted field and its spatial derivatives, as well as assign different
499 weights to each type of data. The Euler inversion algorithm is computationally efficient because
500 most of the large matrices involved in the computations are diagonal or block-diagonal. We
501 found that, in practice, the computation time of Euler inversion and Euler deconvolution are on
502 the same order of magnitude.

503 Tests on synthetic data show that Euler inversion outperforms Euler deconvolution and
504 finite-difference Euler deconvolution (a variant that estimates η but does not rely on second-order
505 derivatives) in terms of robustness to random noise and interfering sources inside the data
506 window. Our tests also show that the estimated z_o coordinate is correlated with the structural
507 index, as is the case for Euler deconvolution. We have also found that the data misfit from Euler
508 inversion is minimal when the used integer structural index is equal or close to the true one. This
509 led us to develop an algorithm for estimating the best integer structural index based on the data
510 misfit. A test on complex synthetic data from a model of dykes and dipoles with overlapping
511 signals shows that Euler inversion is able to estimate the structural index and position of the
512 sources within expected error bounds when the signal overlap is not larger than the data window.
513 For deeper dykes in particular, Euler inversion was not able to estimate the correct $\eta = 1$, leading
514 to an overestimation of the depths.

515 We applied Euler inversion to an aeromagnetic dataset from Rio de Janeiro, Brazil, to analyse
516 its performance under real-world scenarios. Euler inversion was able to locate the NE-SW linear
517 features in the data with an $\eta = 1$ which are associated with known dyke outcrops. For the
518 deeper linear features, Euler inversion was not able to estimate the correct $\eta = 1$. Some of the
519 dipolar anomalies present in the data were picked out with $\eta = 3$, while the sources with a
520 large signal overlap with other features provided a mix of $\eta = 2$ and $\eta = 3$. These results are
521 consistent with the synthetic data tests and show the benefits and limitations of the proposed
522 method.

523 Euler inversion outperforms other Euler-based methods in most cases. However, it still suffers
524 from some of the same limitations. While Euler inversion is less sensitive to signal overlap,
525 it still fails to correctly estimate the position and structural index when the overlap is large.

526 The windowing procedure still generates a large amount of spurious solutions which need to be
527 filtered out. This could be improved with techniques like the source detection method proposed
528 by Castro et al. (2020), for example. Euler inversion can also be coupled with other inverse
529 problems by following our methodology to add Euler's equation as a non-linear constraint. This
530 could help with issues of non-uniqueness and stability in traditional 3D inverse problems in
531 potential-field methods.

532 Open research

533 The Python source code and data that were used to produce all results and figures presented
534 here are available at <https://github.com/compgeolab/euler-inversion> and <https://doi.org/10.6084/m9.figshare.26384140> (Uieda et al., 2024) under the CC-BY license and the MIT license. This
535 study made use of the following open-source scientific software: matplotlib (Hunter, 2007) and
536 PyGMT (Tian et al., 2024) for generating figures and maps, Numpy (Harris et al., 2020) and
537 Scipy (Virtanen et al., 2020) for linear algebra, Pandas for manipulating tabular data (McKinney,
538 2010; The pandas development team, 2024), GeoPandas for reading and plotting shapefiles (den
539 Bossche et al., 2024), pyproj for data projection (Snow et al., 2024), xarray (Hoyer and Hamman,
540 2017) for working with gridded data, Verde (Uieda, 2018) for moving windows and interpolation,
541 and Harmonica (Fatiando a Terra Project et al., 2023) for potential-field data processing and
542 modeling. The aeromagnetic and geologic data are available from Serviço Geológico do Brasil
543 (<https://geosgb.sgb.gov.br>) under a CC-BY-NC license. The magnetic data are part of survey
544 1038 “Projeto Aerogeofísico São Paulo – Rio de Janeiro”. Both are also available in our source
545 code and data archive (Uieda et al., 2024).

547 Acknowledgements

548 We are indebted to the developers and maintainers of the open-source software without which
549 this work would not have been possible. LU would like to thank Prof. Spiros Pagiatakis for
550 being an incredible instructor and teaching him the mathematics which formed the foundations

551 of this work during his undergraduate exchange at York University. LU was supported in part
552 by start-up grant PRPI 22.1.09345.01.2 from Universidade de São Paulo. GFSJ was supported
553 by scholarship 2021/08379-5 from the Fundação de Amparo à Pesquisa do Estado de São Paulo
554 (FAPESP). The opinions, hypotheses, and conclusions or recommendations expressed in this
555 material are the responsibility of the authors and do not necessarily reflect the views of FAPESP.

556 CRediT author contributions

557 **Leonardo Uieda:** Conceptualisation, Data curation, Formal analysis, Investigation, Methodol-
558 ogy, Project administration, Resources, Software, Supervision, Visualisation, Writing – original
559 draft. **Gelson Ferreira Souza-Junior:** Data curation, Formal analysis, Resources, Software,
560 Visualisation, Writing - original draft, Writing - review & editing. **India Uppal:** Data cura-
561 tion, Formal analysis, Investigation, Software, Writing - review & editing. **Vanderlei Coelho**
562 **Oliveira Jr.:** Conceptualisation, Methodology, Writing - review & editing.

563 References

- 564 Almeida, J., Dios, F., Mohriak, W., Valeriano, C., Heilbron, M., Eirado, L., and Tomazzoli, E.
565 (2013). Pre-rift tectonic scenario of the eo-cretaceous gondwana break-up along se brazil –
566 sw africa insights from tholeiitic mafic dykes swarms. In *Geological Society, London, Special*
567 *Publications*, volume 369, pages 11–40. Geological Society of London.
- 568 Aster, R. C., Borchers, B., and Thurber, C. H. (2018). *Parameter estimation and inverse*
569 *problems*. Elsevier.
- 570 Castro, F. R., Oliveira, S. P., de Souza, J., and Ferreira, F. J. F. (2020). Constraining euler
571 deconvolution solutions through combined tilt derivative filters. *Pure and Applied Geophysics*,
572 177(10):4883–4895. doi:[10.1007/s00024-020-02533-w](https://doi.org/10.1007/s00024-020-02533-w). URL <http://dx.doi.org/10.1007/s00024-020-02533-w>.
- 574 Dantas, M. E., Moraes, J. M., Ferrassoli, M. A., Jorge, M. d. Q., and Hilquias, V. A. (2017).

- 575 *Geodiversidade do estado do Rio de Janeiro*. CPRM. URL <https://rigeo.sgb.gov.br/handle/doc/20479>.
- 576
- 577 den Bossche, J. V., Jordahl, K., Fleischmann, M., Richards, M., McBride, J., Wasserman,
578 J., Badaracco, A. G., Snow, A. D., Ward, B., Tratner, J., Gerard, J., Perry, M., cjfqf,
579 Hjelle, G. A., Taves, M., ter Hoeven, E., Cochran, M., Bell, R., rraymondgh, Bartos, M.,
580 Roggemans, P., Culbertson, L., Caria, G., Tan, N. Y., Eubank, N., sangershanan, Flavin,
581 J., Rey, S., and Gardiner, J. (2024). geopandas/geopandas: v1.0.1 [software]. *Zenodo*.
582 doi:[10.5281/ZENODO.12625316](https://doi.org/10.5281/ZENODO.12625316).
- 583 Earth Resources Observation And Science (EROS) Center (2017). Shuttle radar topography
584 mission (srtm) 1 arc-second global. doi:[10.5066/F7PR7TFT](https://doi.org/10.5066/F7PR7TFT). URL https://www.usgs.gov/centers/eros/science/usgs-eros-archive-digital-elevation-shuttle-radar-topography-mission-srtm-1-arc?qt-science_center_objects=0#qt-science_center_objects.
- 585
- 586
- 587 Egydio-Silva, M., Vauchez, A., Raposo, M., Bascou, J., and Uhlein, A. (2005). Deformation
588 regime variations in an arcuate transpressional orogen (ribeira belt, se brazil) imaged by
589 anisotropy of magnetic susceptibility in granulites. *Journal of Structural Geology*, 27:1750–1764.
590 doi:[10.1016/j.jsg.2005.03.010](https://doi.org/10.1016/j.jsg.2005.03.010).
- 591 Fatiando a Terra Project, Esteban, F. D., Li, L., Oliveira Jr, V. C., Pesce, A., Shea, N., Soler,
592 S. R., Tankersley, M., and Uieda, L. (2023). Harmonica v0.6.0: Forward modeling, inversion,
593 and processing gravity and magnetic data [Software]. *Zenodo*. doi:[10.5281/zenodo.7690145](https://doi.org/10.5281/zenodo.7690145).
- 594 FitzGerald, D., Reid, A., and McInerney, P. (2004). New discrimination techniques for euler
595 deconvolution. *Computers & Geosciences*, 30(5):461–469. doi:[10.1016/j.cageo.2004.03.006](https://doi.org/10.1016/j.cageo.2004.03.006).
596 URL <http://dx.doi.org/10.1016/j.cageo.2004.03.006>.
- 597 Florio, G. and Fedi, M. (2013). Multiridge euler deconvolution. *Geophysical Prospecting*,
598 62(2):333–351. doi:[10.1111/1365-2478.12078](https://doi.org/10.1111/1365-2478.12078). URL <http://dx.doi.org/10.1111/1365-2478.12078>.
- 599
- 600 Florio, G., Fedi, M., and Paštka, R. (2014). On the estimation of the structural index from
low-pass filtered magnetic data. *GEOPHYSICS*, 79(6):J67–J80. doi:[10.1190/geo2013-0421.1](https://doi.org/10.1190/geo2013-0421.1).
- 601 Gerovska, D., Stavrev, P., and Araúzo-Bravo, M. J. (2005). Finite-difference euler deconvolution
602 algorithm applied to the interpretation of magnetic data from northern bulgaria. *pure and*

- 603 *applied geophysics*, 162(3):591–608. doi:[10.1007/s00024-004-2623-1](https://doi.org/10.1007/s00024-004-2623-1). URL <http://dx.doi.org/10.1007/s00024-004-2623-1>.
- 604
- 605 Harris, C. R., Millman, K. J., van der Walt, S. J., Gommers, R., Virtanen, P., Cournapeau, D.,
606 Wieser, E., Taylor, J., Bergstra, J., Smith, N. J., Kern, R., Picus, M., Hoyer, S., van Kerkwijk,
607 M. H., Brett, M., Haldane, A., Del Río, J., Wiebe, M., Peterson, P., Gérard-Marchant, P.,
608 Sheppard, K., Reddy, T., Weckesser, W., Abbasi, H., Gohlke, C., and Oliphant, T. E. (2020).
609 Array programming with NumPy [software]. *Nature*, 585(7825):357–362. doi:[10.1038/s41586-020-2649-2](https://doi.org/10.1038/s41586-020-2649-2).
- 610
- 611 Heilbron, M., Eirado, L., and Almeida, J. (2016). Mapa geológico e de recursos minerais do
612 estado do rio de janeiro. Programa Geologia do Brasil (PGB), Mapas Geológicos Estaduais.
613 Escala 1:400.000.
- 614 Heilbron, M. and Machado, N. (2003). Timing of terrane accretion in the neoproterozoic-
615 eopaleozoic ribeira orogen (se brazil). *Precambrian Research*, 125(1-2):87–112.
616 doi:[10.1016/S0301-9268\(03\)00082-2](https://doi.org/10.1016/S0301-9268(03)00082-2).
- 617 Heilbron, M., Silva, L. G. d. E., Almeida, J. C. H. d., Tupinambá, M., Peixoto, C., Valeriano,
618 C. d. M., Lobato, M., Rodrigues, S. W. d. O., Ragatky, C. D., Silva, M. A., Monteiro, T.,
619 Freitas, N. C. d., Miguens, D., and Girão, R. (2020). Proterozoic to ordovician geology and
620 tectonic evolution of rio de janeiro state, se-brazil: insights on the central ribeira orogen
621 from the new 1:400,000 scale geologic map. *Brazilian Journal of Geology*, 50(2):e20190099.
622 doi:[10.1590/2317-4889202020190099](https://doi.org/10.1590/2317-4889202020190099).
- 623 Heilbron, M., Valeriano, C. M., Tassinari, C. C. G., Almeida, J., Tupinambá, M., Siga, O., and
624 Trouw, R. (2008). Correlation of neoproterozoic terranes between the ribeira belt, se brazil
625 and its african counterpart: comparative tectonic evolution and open questions. *Geological
626 Society, London, Special Publications*, 294(1):211–237. doi:[10.1144/SP294.12](https://doi.org/10.1144/SP294.12).
- 627 Hoyer, S. and Hamman, J. (2017). xarray: N-D labeled arrays and datasets in Python [software].
628 *Journal of Open Research Software*, 5(1). doi:[10.5334/jors.148](https://doi.org/10.5334/jors.148).
- 629 Huang, L., Zhang, H., Li, C., and Feng, J. (2022). Ratio-euler deconvolution and its applications.
630 *Geophysical Prospecting*, 70(6):1016–1032. doi:[10.1111/1365-2478.13201](https://doi.org/10.1111/1365-2478.13201). URL <http://dx.doi.org/10.1111/1365-2478.13201>

- 631 [rg/10.1111/1365-2478.13201](https://doi.org/10.1111/1365-2478.13201).
- 632 Huang, L., Zhang, H., Sekelani, S., and Wu, Z. (2019). An improved tilt-euler deconvolu-
633 tion and its application on a fe-polymetallic deposit. *Ore Geology Reviews*, 114:103114.
634 doi:[10.1016/j.oregeorev.2019.103114](https://doi.org/10.1016/j.oregeorev.2019.103114). URL <http://dx.doi.org/10.1016/j.oregeorev.2019.103114>.
- 635 Hunter, J. D. (2007). Matplotlib: A 2d graphics environment [software]. *Computing in Science
636 & Engineering*, 9(3):90–95. doi:[10.1109/MCSE.2007.55](https://doi.org/10.1109/MCSE.2007.55).
- 637 McKinney, W. (2010). Data structures for statistical computing in python. In *Proceedings of the
638 9th Python in Science Conference*, SciPy, page 56–61. SciPy. doi:[10.25080/majora-92bf1922-00a](https://doi.org/10.25080/majora-92bf1922-00a).
639 URL <http://dx.doi.org/10.25080/Majora-92bf1922-00a>.
- 640 Meira, V. T., Garcia-Casco, A., Hyppolito, T., Juliani, C., and Schorscher, J. H. D. (2019).
641 Tectono-metamorphic evolution of the central ribeira belt, brazil: A case of late neoproterozoic
642 intracontinental orogeny and flow of partially molten deep crust during the assembly of west
643 gondwana. *Tectonics*, 38:3182–3209. doi:[10.1029/2018TC004959](https://doi.org/10.1029/2018TC004959).
- 644 Meira, V. T., Garcia-Casco, A., Juliani, C., Almeida, R. P., and Schorscher, J. H. D. (2015).
645 The role of intracontinental deformation in supercontinent assembly: Insights from the ribeira
646 belt, southeastern brazil (neoproterozoic western gondwana). *Terra Nova*, 27(3):206–217.
647 doi:[10.1111/ter.12149](https://doi.org/10.1111/ter.12149).
- 648 Melo, F. F. and Barbosa, V. C. (2020). Reliable euler deconvolution estimates throughout
649 the vertical derivatives of the total-field anomaly. *Computers & Geosciences*, 138:104436.
650 doi:[10.1016/j.cageo.2020.104436](https://doi.org/10.1016/j.cageo.2020.104436).
- 651 Melo, F. F. and Barbosa, V. C. F. (2018). Correct structural index in euler deconvolution
652 via base-level estimates. *GEOPHYSICS*, 83(6):J87–J98. doi:[10.1190/geo2017-0774.1](https://doi.org/10.1190/geo2017-0774.1). URL
653 <http://dx.doi.org/10.1190/geo2017-0774.1>.
- 654 Melo, F. F., Barbosa, V. C. F., Uieda, L., Oliveira Jr., V. C., and Silva, J. B. C. (2013).
655 Estimating the nature and the horizontal and vertical positions of 3d magnetic sources
656 using euler deconvolution. *GEOPHYSICS*, 78(6):J87–J98. doi:[10.1190/geo2012-0515.1](https://doi.org/10.1190/geo2012-0515.1). URL
657 <http://dx.doi.org/10.1190/geo2012-0515.1>.
- 658 Pašteka, R., Richter, F., Karcol, R., Brazda, K., and Hajach, M. (2009). Regularized derivatives

- 659 of potential fields and their role in semi-automated interpretation methods. *Geophysical*
660 *Prospecting*, 57(4):507–516. doi:[10.1111/j.1365-2478.2008.00780.x](https://doi.org/10.1111/j.1365-2478.2008.00780.x).
- 661 Reid, A. B., Allsop, J. M., Granser, H., Millett, A. J., and Somerton, I. W. (1990). Magnetic
662 interpretation in three dimensions using Euler deconvolution. *GEOPHYSICS*, 55(1):80–91.
663 doi:[10.1190/1.1442774](https://doi.org/10.1190/1.1442774).
- 664 Reid, A. B., Ebbing, J., and Webb, S. J. (2014). Avoidable euler errors – the use and abuse
665 of euler deconvolution applied to potential fields. *Geophysical Prospecting*, 62(5):1162–1168.
666 doi:[10.1111/1365-2478.12119](https://doi.org/10.1111/1365-2478.12119). URL <http://dx.doi.org/10.1111/1365-2478.12119>.
- 667 Reid, A. B. and Thurston, J. B. (2014). The structural index in gravity and magnetic interpre-
668 tation: Errors, uses, and abuses. *GEOPHYSICS*, 79(4):J61–J66. doi:[10.1190/geo2013-0235.1](https://doi.org/10.1190/geo2013-0235.1).
669 URL <http://dx.doi.org/10.1190/geo2013-0235.1>.
- 670 Ruddock, K. A., Slack, H. A., and Sheldon, B. (1966). Method for determining depth and falloff
671 rate of subterranean magnetic disturbances utilizing a plurality of magnetometers. US Patent
672 3,263,161.
- 673 Saleh, S. and Pašteka, R. (2012). Applying the regularized derivatives approach in euler
674 deconvolution and modeling geophysical data to estimate the deep active structures for
675 the northern red sea rift region, egypt. *Contributions to Geophysics and Geodesy*, 42(1).
676 doi:[10.2478/v10126-012-0003-x](https://doi.org/10.2478/v10126-012-0003-x). URL <http://dx.doi.org/10.2478/v10126-012-0003-x>.
- 677 Salem, A. and Ravat, D. (2003). A combined analytic signal and euler method (an-eul) for auto-
678 matic interpretation of magnetic data. *GEOPHYSICS*, 68(6):1952–1961. doi:[10.1190/1.1635049](https://doi.org/10.1190/1.1635049).
679 URL <http://dx.doi.org/10.1190/1.1635049>.
- 680 Salem, A., Smith, R., Williams, S., Ravat, D., and Fairhead, D. (2007). Generalized magnetic
681 tilt-euler deconvolution. In *SEG Technical Program Expanded Abstracts 2007*, page 790–794.
682 Society of Exploration Geophysicists. doi:[10.1190/1.2792530](https://doi.org/10.1190/1.2792530). URL <http://dx.doi.org/10.1190/1.2792530>.
- 684 Silva, J. B. C. and Barbosa, V. C. F. (2003). 3d euler deconvolution: Theoretical basis for auto-
685 matically selecting good solutions. *GEOPHYSICS*, 68(6):1962–1968. doi:[10.1190/1.1635050](https://doi.org/10.1190/1.1635050).
686 URL <http://dx.doi.org/10.1190/1.1635050>.

- 687 Silva, J. B. C., Barbosa, V. C. F., and Medeiros, W. E. (2001). Scattering, symmetry, and
688 bias analysis of source-position estimates in euler deconvolution and its practical implications.
689 *GEOPHYSICS*, 66(4):1149–1156. doi:[10.1190/1.1487062](https://doi.org/10.1190/1.1487062).
- 690 Snow, A. D., Whitaker, J., Cochran, M., Miara, I., den Bossche, J. V., Mayo, C., Lucas, G.,
691 Cochrane, P., de Kloe, J., Karney, C., Shaw, J. J., Filipe, Ouzounoudis, G., Dearing, J., Lostis,
692 G., Hoese, D., Couwenberg, B., Jurd, B., Gohlke, C., Schnell, C., McDonald, D., Itkin, M.,
693 May, R., de Bittencourt, H., Little, B., Rahul, P. S., Eubank, N., Neil, and Taves, M. (2024).
694 pyproj4/pyproj: 3.7.0 release [software]. *Zenodo*. doi:[10.5281/ZENODO.13864781](https://doi.org/10.5281/ZENODO.13864781).
- 695 Soler, S. R. and Uieda, L. (2021). Gradient-boosted equivalent sources. *Geophysical Journal
696 International*, 227(3):1768–1783. doi:[10.1093/gji/ggab297](https://doi.org/10.1093/gji/ggab297). URL <http://dx.doi.org/10.1093/gji/ggab297>.
- 697 Stavrev, P. and Reid, A. (2007). Degrees of homogeneity of potential fields and structural
698 indices of euler deconvolution. *GEOPHYSICS*, 72(1):L1–L12. doi:[10.1190/1.2400010](https://doi.org/10.1190/1.2400010). URL
700 <http://dx.doi.org/10.1190/1.2400010>.
- 701 The pandas development team (2024). pandas-dev/pandas: Pandas [software]. *Zenodo*.
702 doi:[10.5281/ZENODO.13819579](https://doi.org/10.5281/ZENODO.13819579).
- 703 Thompson, D. T. (1982). Euldhph: a new technique for making computer-assisted depth estimates
704 from magnetic data. *Geophysics*, 47(1):31–37. doi:[10.1190/1.1441278](https://doi.org/10.1190/1.1441278).
- 705 Thompson, R. N., Gibson, S. A., Mitchell, J. G., Dickin, A. P., Leonards, O. H., Brod, J. A.,
706 and Greenwood, J. C. (1998). Migrating Cretaceous–Eocene Magmatism in the Serra do Mar
707 Alkaline Province, SE Brazil: Melts from the Deflected Trindade Mantle Plume? *Journal of
708 Petrology*, 39(8):1493–1526. doi:[10.1093/petroj/39.8.1493](https://doi.org/10.1093/petroj/39.8.1493).
- 709 Tian, D., Uieda, L., Leong, W. J., Fröhlich, Y., Schlitzer, W., Grund, M., Jones, M., Toney, L.,
710 Yao, J., Magen, Y., Jing-Hui, T., Materna, K., Belem, A., Newton, T., Anant, A., Ziebarth,
711 M., Quinn, J., and Wessel, P. (2024). Pygmt: A python interface for the generic mapping
712 tools [software]. doi:[10.5281/ZENODO.3781524](https://doi.org/10.5281/ZENODO.3781524).
- 713 Trouw, R., Heilbron, M., Ribeiro, A., Paciullo, F., Valeriano, C., Almeida, J., Tupinambá, M.,
714 and Andreis, R. (2000). The central segment of the ribeira belt. In Cordani, U., Milani, E.,

- 715 Thomaz Filho, A., and Campos, D., editors, *Geotectonics of South America*, pages 297–310.
- 716 31st International Geological Congress (IGC), Special Publication.
- 717 Uieda, L. (2018). Verde: Processing and gridding spatial data using Green's functions [software].
718 *Journal of Open Source Software*, 3(29):957. doi:[10.21105/joss.00957](https://doi.org/10.21105/joss.00957).
- 719 Uieda, L., Oliveira, V., and Barbosa, V. (2013). Modeling the earth with fatiando a
720 terra. In *Proceedings of the 12th Python in Science Conference*, SciPy, page 92–98. SciPy.
721 doi:[10.25080/majora-8b375195-010](https://doi.org/10.25080/majora-8b375195-010). URL <http://dx.doi.org/10.25080/Majora-8b375195-010>.
- 722 Uieda, L., Oliveira, V. C., and Barbosa, V. C. F. (2014). Geophysical tutorial: Euler deconvolution
723 of potential-field data. *The Leading Edge*, 33(4):448–450. doi:[10.1190/tle33040448.1](https://doi.org/10.1190/tle33040448.1). URL
724 <http://dx.doi.org/10.1190/tle33040448.1>.
- 725 Uieda, L., Souza-Junior, G. F., Uppal, I., and Oliveira Jr., V. C. (2024). Supplementary material
726 for “Euler inversion: Locating sources of potential-field data through inversion of Euler’s
727 homogeneity equation” [Dataset]. doi:[10.6084/m9.figshare.26384140](https://doi.org/10.6084/m9.figshare.26384140).
- 728 Valeriano, C., Tupinambá, M., Simonetti, A., Heilbron, M., Almeida, J., and Eirado Silva,
729 L. (2011). U-pb la-mc-icpms geochronology of cambro-ordovician post-collisional gran-
730 ites of the ribeira belt, southeast brazil: terminal brasiliense magmatism in central
731 gondwana supercontinent. *Journal of South American Earth Sciences*, 32(4):416–428.
732 doi:[10.1016/j.jsames.2011.03.003](https://doi.org/10.1016/j.jsames.2011.03.003).
- 733 Van Huffel, S. and Vandewalle, J. (1991). *The Total Least Squares Problem: Computational
734 Aspects and Analysis*. Society for Industrial and Applied Mathematics. ISBN 9781611971002.
735 doi:[10.1137/1.9781611971002](https://doi.org/10.1137/1.9781611971002).
- 736 Vanícek, P. and Krakiwsky, E. (1986). *Geodesy: The Concepts*. Elsevier Science.
- 737 Virtanen, P., Gommers, R., Oliphant, T. E., Haberland, M., Reddy, T., Cournapeau, D.,
738 Burovski, E., Peterson, P., Weckesser, W., Bright, J., van der Walt, S. J., Brett, M., Wilson,
739 J., Millman, K. J., Mayorov, N., Nelson, A. R. J., Jones, E., Kern, R., Larson, E., Carey, C. J.,
740 Polat, I., Feng, Y., Moore, E. W., VanderPlas, J., Laxalde, D., Perktold, J., Cimrman, R.,
741 Henriksen, I., Quintero, E. A., Harris, C. R., Archibald, A. M., Ribeiro, A. H., Pedregosa, F.,
742 van Mulbregt, P., and Contributors (2020). SciPy 1.0: Fundamental Algorithms for Scientific

- 743 Computing in Python [Software]. *Nature Methods*, 17(3):261–272. doi:[10.1038/s41592-019-0686-2](https://doi.org/10.1038/s41592-019-0686-2).
- 744
- 745 Wells, D. and Krakiwsky, E. (1971). *The method of least squares*. Number 18. Department of
746 Geodesy and Geomatics Engineering Lecture Notes, University of New Brunswick.